Supporting Information

Construction of two drug-loaded gold nanoclusters@mesoporous polydopamine nanospheres and their synergistic treatment of abdominal aortic aneurysms

Wenhao Li[1], Weina Zhang[1], Qin Huang[1], Mengjie Xu[1], Dehong Wu[1], Qi Hu[1], Dianwu Wu[2]*, Guangfu Yin[1], Zhongbing Huang[1]*

1. College of Biomedical Engineering, Sichuan University, Chengdu, 610065, China
2. Institute of Energy, Hefei Comprehensive National Science Center (Anhui Energy Laboratory), Hefei, 230088, China

Email: zbhuang@scu.edu.cn (Zhongbing Huang)

wudianwu@ie.ah.cn (Dianwu Wu)

1. Experimental Method

1.1. Investigation of optimal drug-loading conditions

The orthogonal experimental design method was employed to systematically investigate the effects of feed ratio of CTS and TMP, reaction concentration, and reaction time on the drug-loading efficiency. A three-factor, three-level of L9 (3^3) orthogonal array was designed with the aim of optimizing the drug-loading protocol for AuM. The detailed experimental layout is shown in Table S2. Additionally, the influence of the order of adding CTS and TMP on the drug-loading performance of CT-AuM was examined.

1.2. Photothermal conversion efficiency

Photothermal conversion efficiency (PCE, η) is a crucial parameter, which represents the photothermal properties. To evaluate the PCE of AuM, 1 mL of 500 μg/mL of AuM aqueous solution was irradiated by a NIR-II light of 1064 nm of wavelength at 1 W/cm^2 in a quartz colourimetric dish. The irradiation was removed until the temperature climbed to the maximum point and remained constant, and then the solution was naturally cooled to room temperature. During this process, the temperature was observed through a thermocouple digital thermometer every 1 s. Ultimately, PCE (η) can be calculated by the following classical equation: [1,2]

$$\eta = \frac{hS(T_{Max} - T_{Surr}) - Q_{dis}}{I\left(1 - 10^{-A_\lambda}\right)} \tag{1}$$

where h is the heat transfer coefficient, which is obtained through equation (1). S is the surface area of the cuvette, T_{Max} is the temperature of sample aqueous solution at the maximum steady-state, T_{Surr} represents the surrounding temperature, Q_{dis} means the heat dissipated from light absorbed by the quartz colourimetric dish and solvent, I refers to the applied laser power, A_λ is the absorbance of the solution at 1064 nm.

$$\tau_s = \frac{\sum_i m_i C_{p,i}}{hS} \tag{2}$$

$$t = -\tau_s ln(\theta) \tag{3}$$

$$\theta = \frac{T - T_{surr}}{T_{Max} - T_{surr}} \quad (4)$$

In equation (2), m_i and $C_{p,i}$ are the mass and heat capacity of the water. τ_s is the system time constant, defined as the slope of cooling time t against $-ln(\theta)$, where θ is the temperature driving force, as defined by equations (3), (4), respectively.

1.3. Cyto-compatibility

The cyto-compatibility of AuM, T-AuM and CT-AuM was evaluated with the cell counting kit-8 (CCK-8) assay. Human umbilical vein endothelial cells (HUVECs) and mouse monocyte-macrophage cells (RAW264.7) were cultured in Dulbecco's Modified Eagle Medium (DMEM) supplemented with 10% fetal bovine serum and 1% penicillin-streptomycin in a humidified incubator at 37 ℃ with 5% CO_2. Primary vascular smooth muscle cells (VSMCs, provided by West China Hospital, Sichuan University) were cultured in a 1:1 mixture of DMEM and Ham's F-12 medium (DMEM/F-12) containing 20% fetal bovine serum and 1% penicillin-streptomycin under the same incubation conditions.

In a 96-well plate, HUVECs, RAW264.7, and VSMCs were seeded at 5 × 10^4, 1 × 10^6, and 2.5 × 10^4 cells/mL, respectively. After 24 h of adhesion, the culture medium was replaced with medium containing different concentrations of the materials (0, 12.5, 25, 50, 75, and 100 μg/mL, respectively). At days 1, 2, and 3 of co-culture, the original medium was discarded, and medium containing 10% CCK-8 reagent was added and incubated for 1-3 h. The absorbance of the reaction product was measured at a wavelength of 450 nm. Cell viability was calculated according to the following formula (5):

$$Cell\ viability\ （\%）= \frac{OD_{EXP} - OD_{NEG}}{OD_{CON} - OD_{NEG}} \times 100\% \quad (5)$$

where OD_{EXP}, OD_{CON}, and OD_{NEG} represent the absorbance of the experimental sample, the control sample, and the negative control (cell-free) sample, respectively.

In a 96-well plate, HUVECs, RAW264.7, and VSMCs were seeded at 5 × 10^4, 1 × 10^6, and 2.5 × 10^4 cells/mL, respectively. After 24 h of adhesion, the culture medium was replaced with medium containing different concentrations of the materials (0, 12.5, 25, 50, 75, and 100 μg/mL, respectively). At days 1, 2, and 3 of co-culture, the original medium was discarded, and 100 μL of a staining solution prepared in PBS (containing 2 μM of Calcein-AM and 4 μM of propidium iodide) was added into each well. The plates were incubated at 37 ℃ in the dark for 20 min. After incubation, the staining solution was removed, and the cells

were gently washed once with PBS before immediate observation under a fluorescence microscope. Live cells stained with Calcein-AM (green fluorescence) were observed using the green fluorescence channel (excitation/emission ≈ 490/515 nm of wavelength), and dead cells stained with propidium iodide (red fluorescence) were observed using the red fluorescence channel (excitation/emission ≈ 535/617 nm of wavelength).

1.4. Ultrasonographic evaluation of AAA model[3]

Abdominal ultrasound imaging is one of the standard diagnostic methods for AAA. The assessment primarily relies on three key parameters: the maximum average aortic diameter, the circumferential cyclic strain of the vessel wall, and the blood flow velocity. Generally, a larger maximum average aortic diameter, a lower circumferential cyclic strain of the vessel wall, and a slower blood flow velocity indicate a more severe AAA condition. The calculation formulas (6) and (7) for the maximum average aortic diameter and the circumferential cyclic strain of the vessel wall are as follows:

$$D_M = \frac{1}{3}(D_S - D_D) + D_D \tag{6}$$

$$Circumferential\ cyclic\ strain = \frac{1}{2}\left(\frac{D_S}{D_D} - 1\right)^2 \times 100\% \tag{7}$$

In the formula (6) and (7), D_S represents the aortic internal diameter during systole, and D_D represents the aortic internal diameter during diastole.

2. Information of the experimental materials

Detailed information of the experimental materials used is provided in Table S1.

Table S1. Information of the experimental materials

Name	Purity/Specification	Manufacturer
Pluronic F-127	AR	American sigma Company
1,3,5-Trimethylbenzene (TMB)	≥98%	Shanghai Aladdin Biochemical Technology Co., LTD
Dopamine (DA)	99%	American sigma Company
$HAuCl_4 \cdot 3H_2O$	99.9%	Shanghai Aladdin Biochemical Technology Co., LTD
Tris(hydroxymethyl)aminomethane (Tris)	99.5%	German BioFROXX Company
$NH_3 \cdot H_2O$	25%～28%	Chengdu Kelong Chemicals Co., LTD
Ligustrazine (TMP)	98%	Shanghai Maclean Biochemical Technology Co., LTD
Cryptotanshinone (CTS)	≥98%	Shanghai Aladdin Biochemical Technology Co., LTD
Ring (arginine-glycine-aspartic acid-D-phenylalanine-lysine) (referred to as c(RGDfK))	≥98%	Guangzhou Weihua Biotechnology Co., LTD
Calcein/PI Cell Activity/Toxicity Detection Kit	Biological grade	Shanghai Biyun Tian Biotechnology Co., LTD
Lipopolysaccharide (LPS)	Biological grade	Shanghai Biyun Tian Biotechnology Co., LTD
Platelet-derived growth factor -BB	Biological grade	Suzhou Sunnovo Protein Science & Technology Co., LTD
TNF-α enzyme-linked immunosorbent assay kit	Biological grade	Wuhan Finn Biotechnology Co., LTD
IL-6 enzyme-linked immunosorbent assay kit	Biological grade	Wuhan Finn Biotechnology Co., LTD
IL-1β enzyme-linked immunosorbent assay kit	Biological grade	Wuhan Finn Biotechnology Co., LTD
IL-10 enzyme-linked immunosorbent assay kit	Biological grade	Shanghai Enzyme-Linked Biotechnology Co., LTD
α-SMA enzyme-linked immunosorbent assay kit	Biological grade	Shanghai Jianglai Biotechnology Co., LTD
Tribromoethanol	Biological grade	Shanghai Adamas Reagent Co., LTD
Anhydrous $CaCl_2$	96%	Shanghai Maclean Biochemical Technology Co., LTD

3. Results

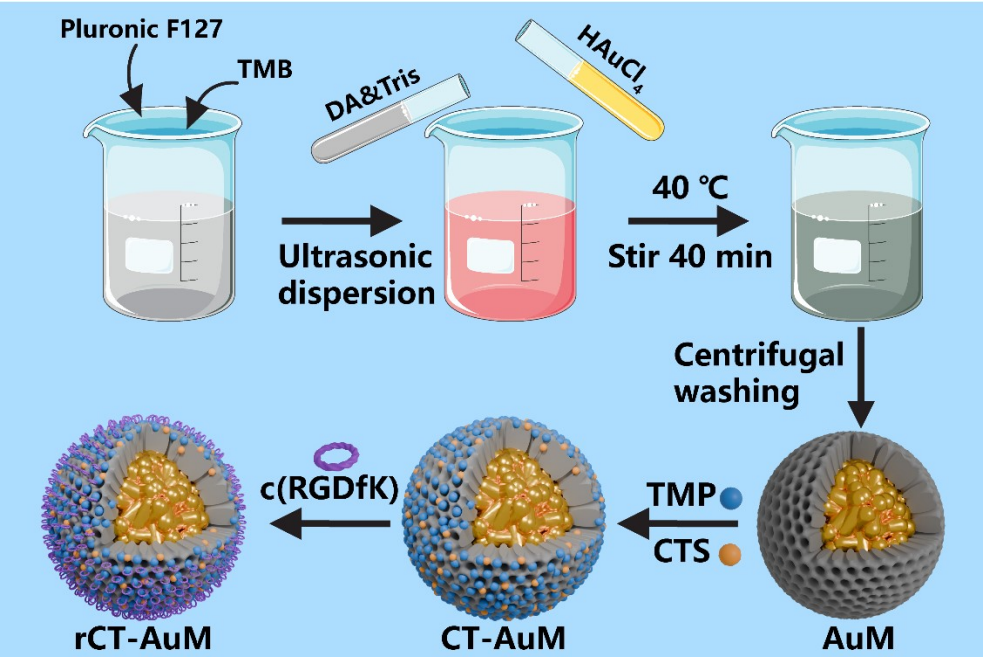

Figure S1. Schematic illustration of the preparation process of rCT-AuM

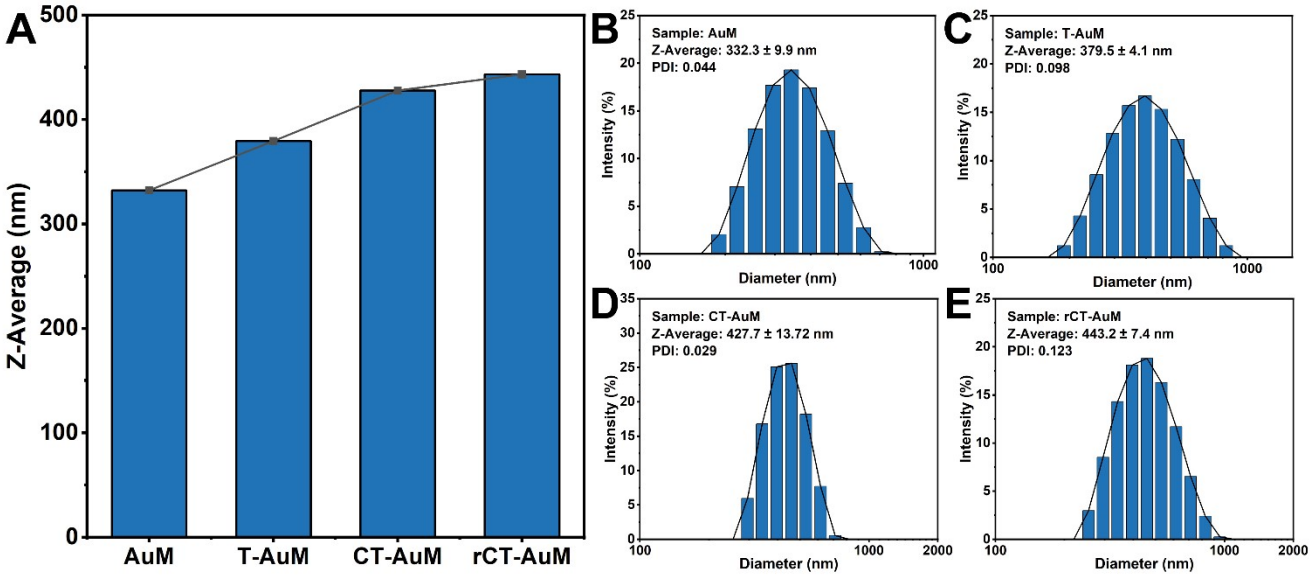

Figure S2. Particle sizes of materials at each stage: (A) comparison of different materials, (B) AuM, (C) T-AuM, (D) CT-AuM and (E) rCT-AuM

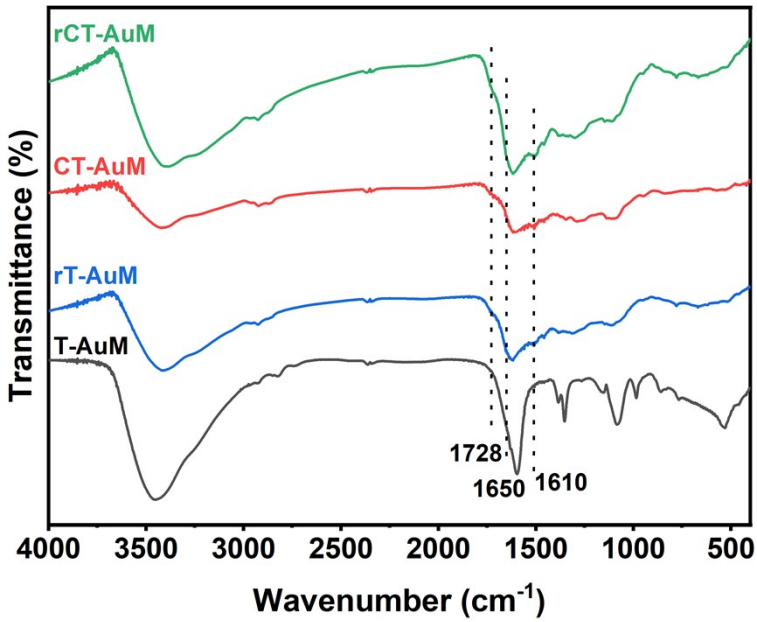

Figure S3. FT-IR spectra of T-AuM and CT-AuM before and after targeted modification

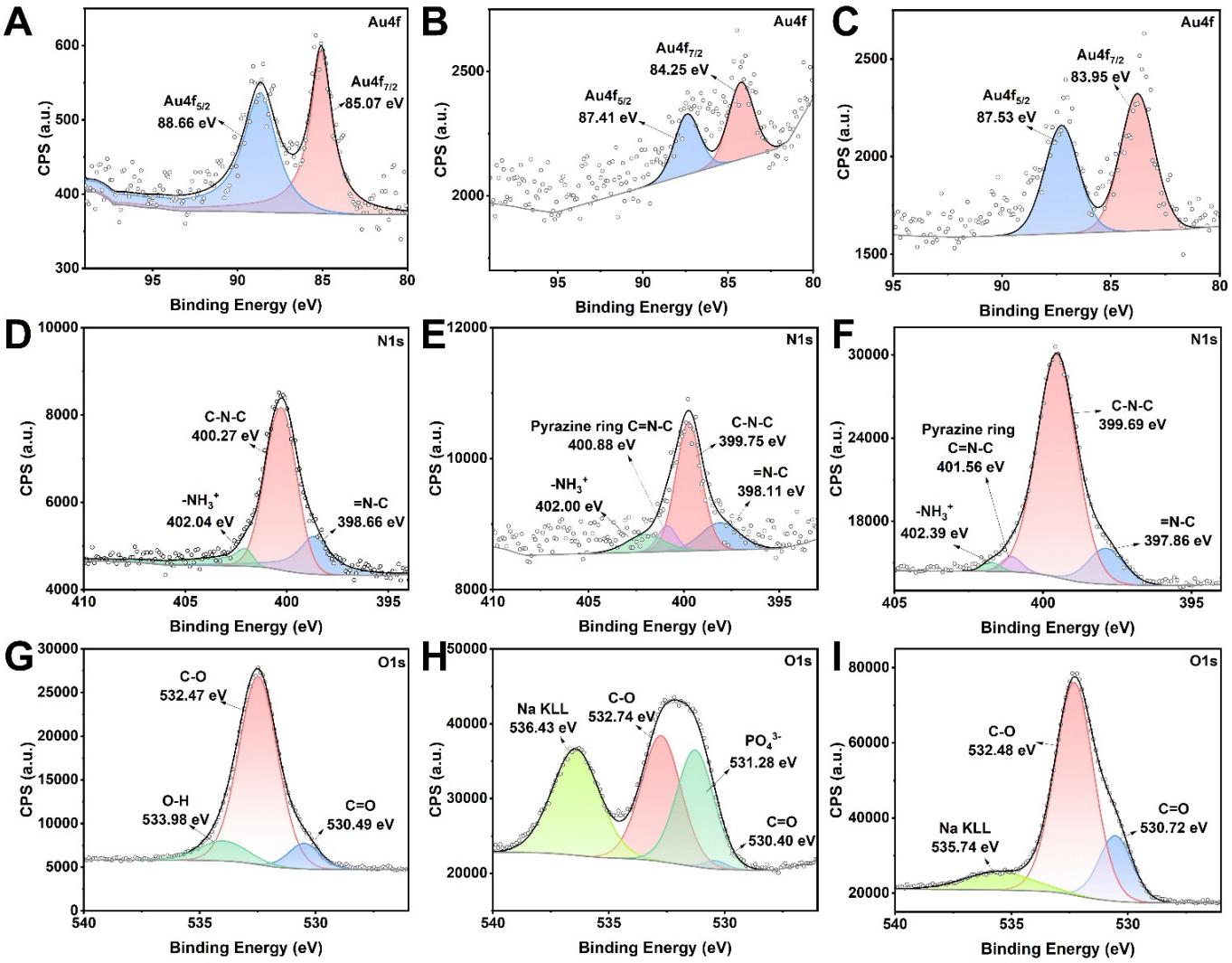

Figure S4. XPS spectra of materials at each stage: Au4f of (A) AuM, (B) T-AuM and (C) CT-AuM; N1s of (D) AuM, (E) T-AuM and (F) CT-AuM; O1s of (G) AuM, (H) T-AuM and (I) CT-AuM

Table S1. Atomic ratio of C, N, O, Au and π-π in AuM, T-AuM and CT-AuM

	At. (π-π)%	At. (C)%	At. (N)%	At. (O)%	At. (Au)%
AuM	**0.58**	**48.6**	**7.47**	**43.86**	**0.07**
T-AuM	**1.58**	**53.37**	**5.08**	**41.46**	**0.08**
CT-AuM	**1.74**	**49.8**	**8.1**	**42.05**	**0.06**

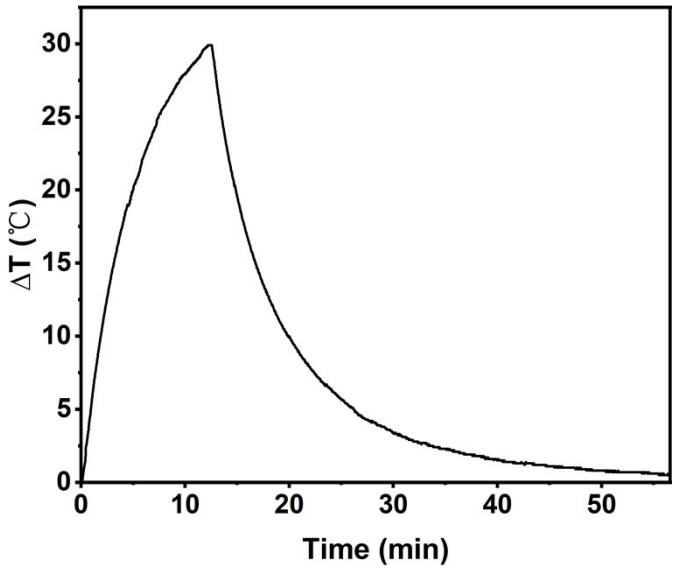

Figure S5. Curve of natural cooling after AuM is heated to the limiting temperature

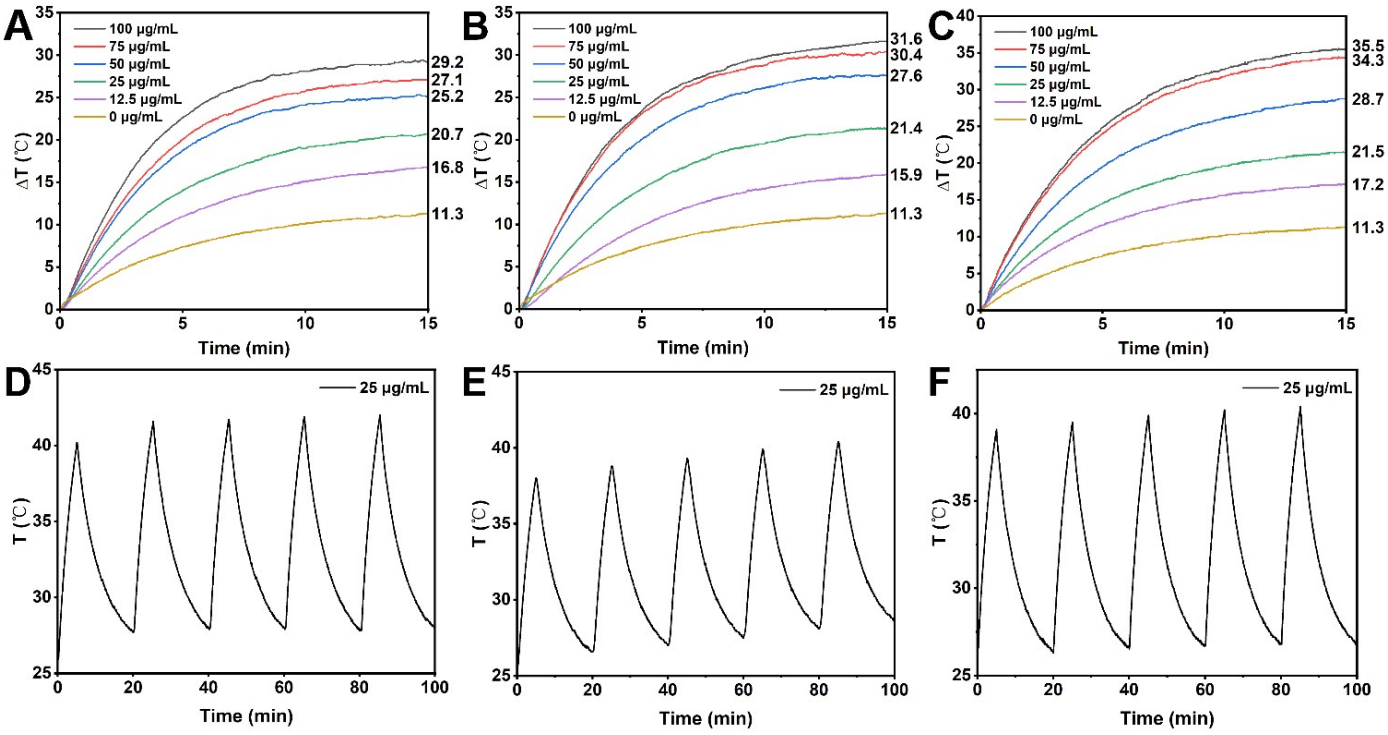

Figure S6. Heating curves of (A) AuM, (B) T-AuM and (C) CT-AuM with different concentration. And photothermal cycle patterns of (D) AuM, (E) T-AuM and (F) CT-AuM with 5 times of NIR-II irradiation (power is 1W/cm^2)

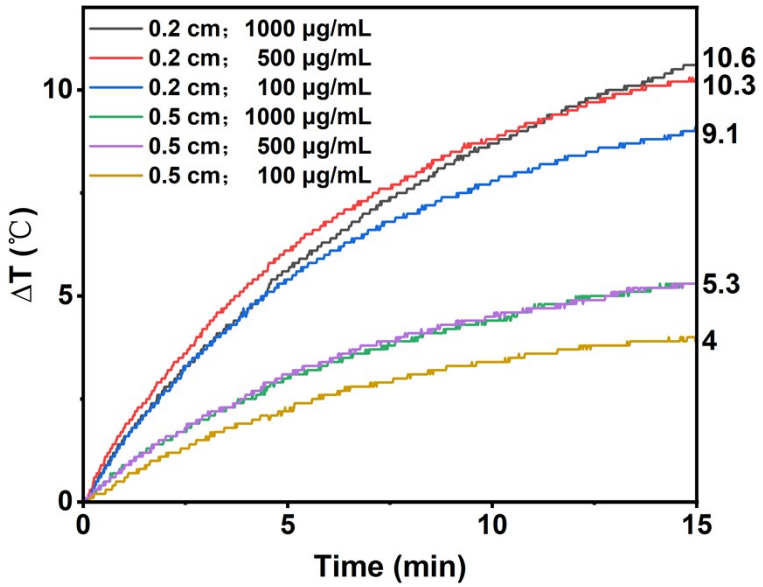

Figure S7. Heating effect of different concentration of CT-AuM with/without rat skin underlying tissue

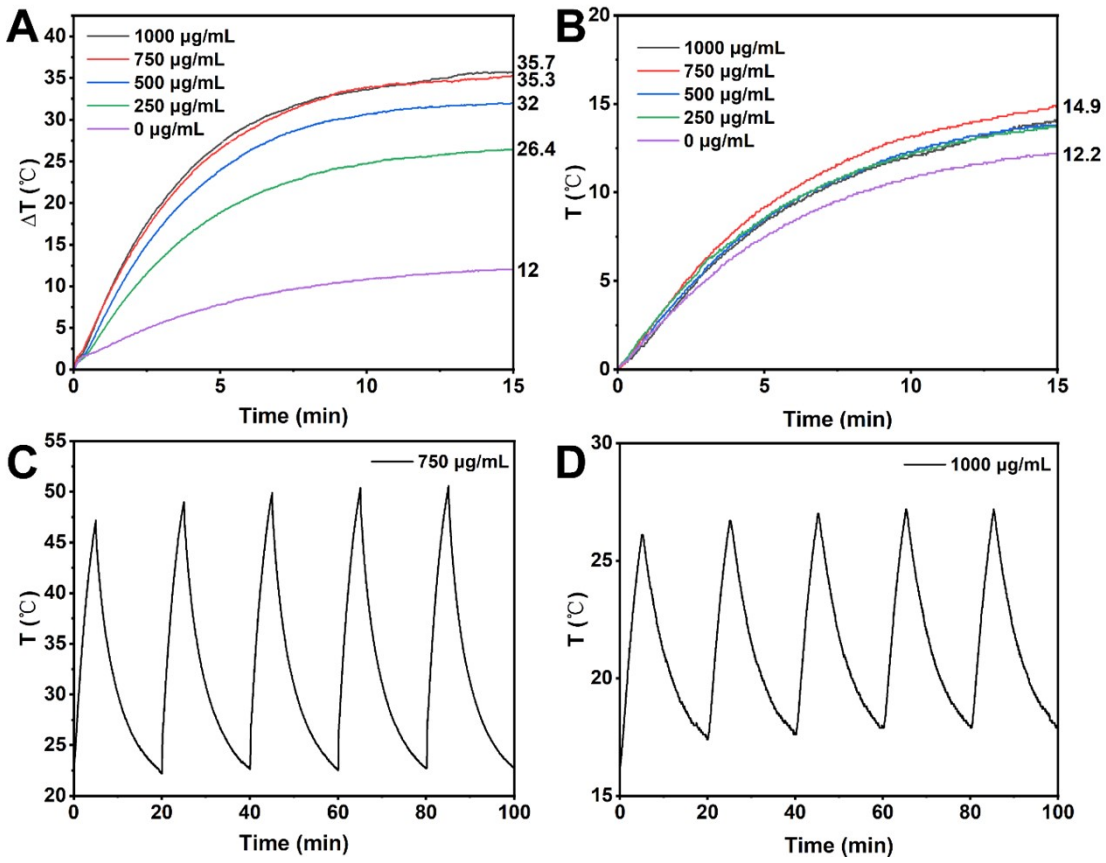

Figure S8. Photothermal heating curves at different concentrations and photothermal stability of (A, C) AuM and corresponding (B, D) Au nanoparticles after mPDA digestion

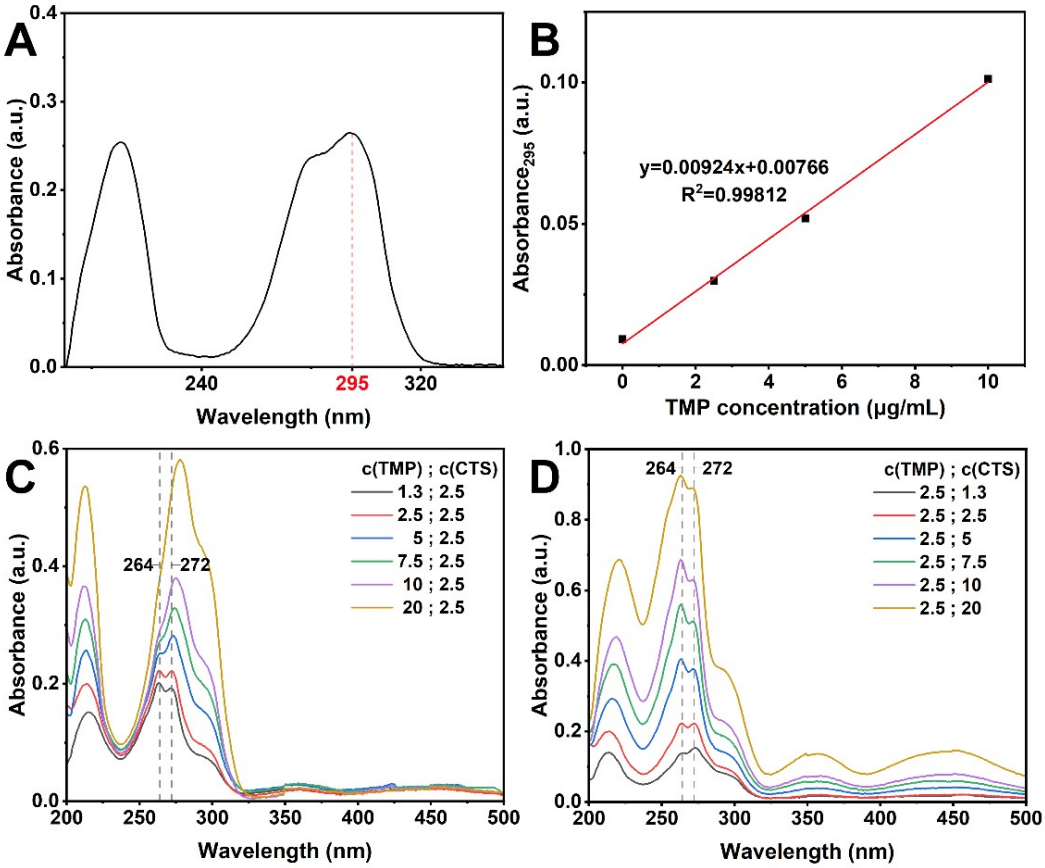

Figure S9. (A) Ultraviolet (UV) absorption spectrum of TMP. (B) Standard line for the relationship between absorbance and concentration of TMP at 295 nm of wavelength. UV absorption spectra of mixtures of TMP/CTS with different concentrations: (C) a fixed concentration of 2.5 mg/mL of CTS; (D) a fixed concentration of 2.5 mg/mL of TMP

Table S2. Orthogonal design of drug-loading efficiency under different conditions.

No.	m_{AuM} : m_{drug} (mg)	reaction concentration (mg/mL)	reaction time (h)
1	1:1	0.5	12
2	1:1	1	24
3	1:1	2	48
4	2:1	0.5	24
5	2:1	1	48
6	2:1	2	12
7	4:1	0.5	48
8	4:1	1	12
9	4:1	2	24

To optimize the drug loading process, an orthogonal experimental design as shown in Table S2 was adopted, and the results are presented in Figure S9. From the perspective of the AuM-to-TMP feed mass ratio: as the proportion of AuM increased, the proportion of TMP decreased accordingly. Although AuM provided more binding sites for drug attachment, the total amount of drug was reduced, leading to a decrease in drug loading capacity but an increase in encapsulation efficiency. To ensure better performance of the material per unit mass in subsequent in vitro and in vivo experiments, an AuM-to-TMP feed mass ratio of 1:1 was selected. From the perspective of the total system concentration: as the total concentration increased, the collision and contact opportunities between AuM and TMP in the stirred system increased, resulting in enhanced both drug loading capacity and encapsulation efficiency. Therefore, a total system concentration of 2 mg/mL was chosen. From the perspective of reaction time: the adsorption and binding between AuM and TMP is a dynamic adsorption-desorption equilibrium process that changes with reaction time. The results showed that the maximum drug loading capacity and encapsulation efficiency were achieved at 48 h. Further prolonging the reaction time would increase the time cost; thus, no longer reaction times were explored, and 48 h was selected as the optimal reaction time.

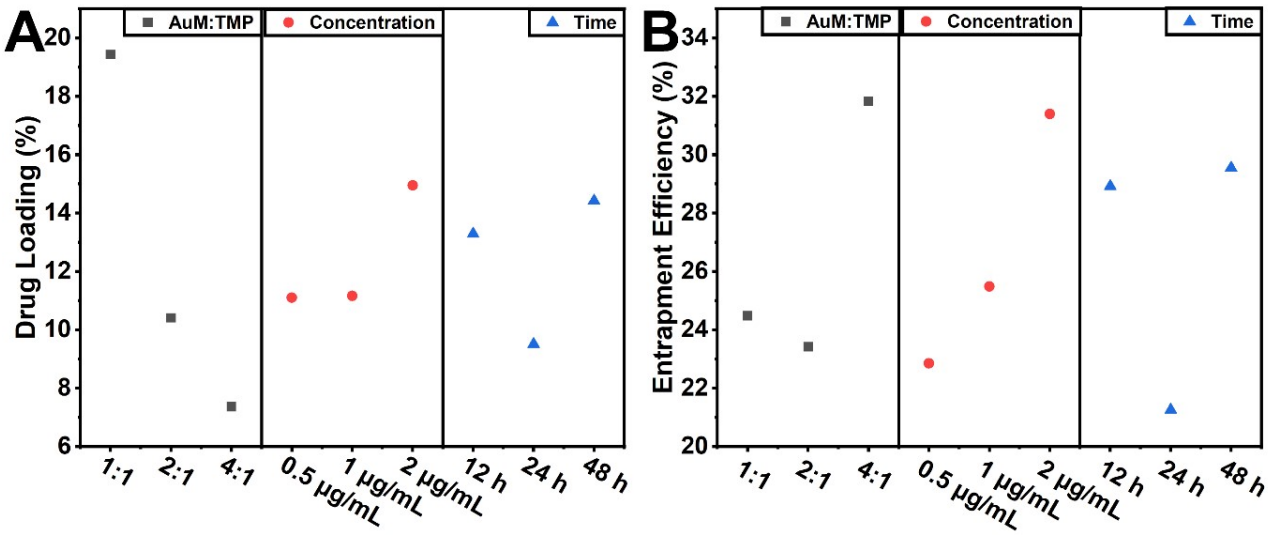

Figure S10. Range plots of orthogonal results: (A) drug loading, (B) entrapment efficiency with different AuM : TMP, reaction concentration and time

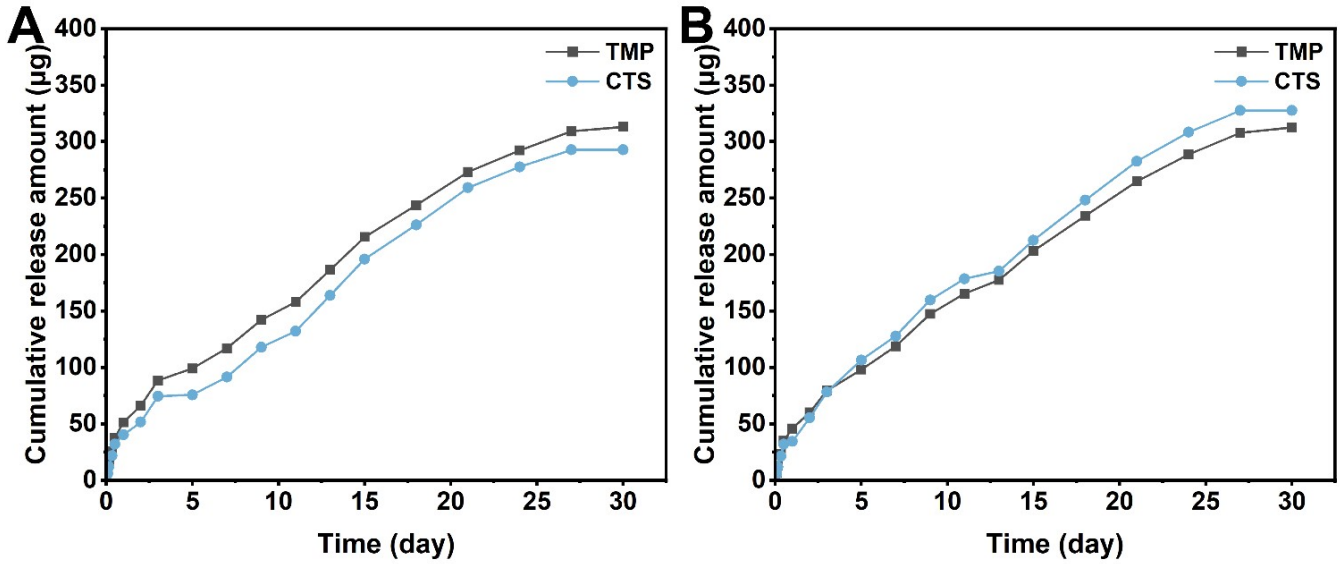

Figure S11. Effect of drug adding sequence during preparation on loading efficiency: (A) TMP added prior to CTS, (B) CTS added prior to TMP

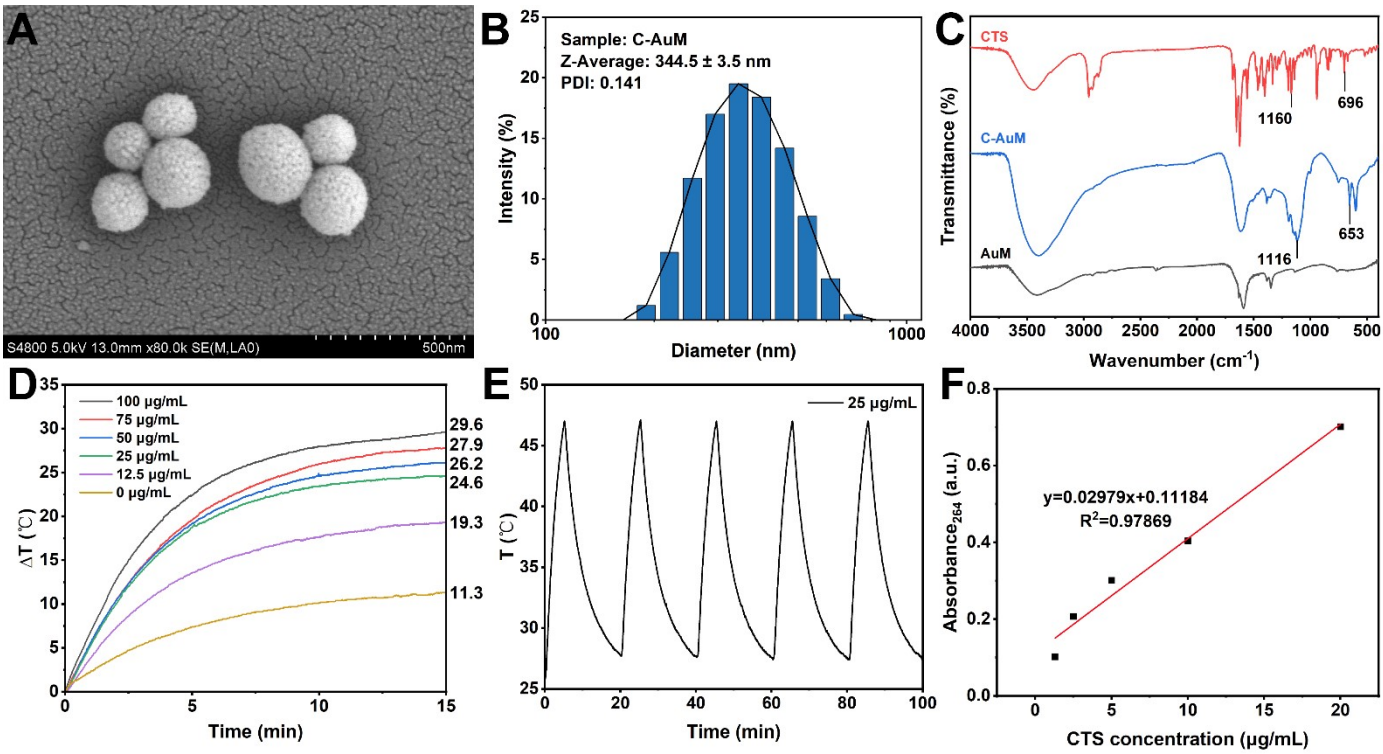

Figure S12. Characterization results of C-AuM: (A) SEM image; (B) Particle size distribution; (C) FT-IR spectrum; (D) Photothermal heating curves at different concentrations; (E) Photothermal cycling stability; (F) Standard line for the relationship between absorbance and concentration of CTS at 264 nm of wavelength

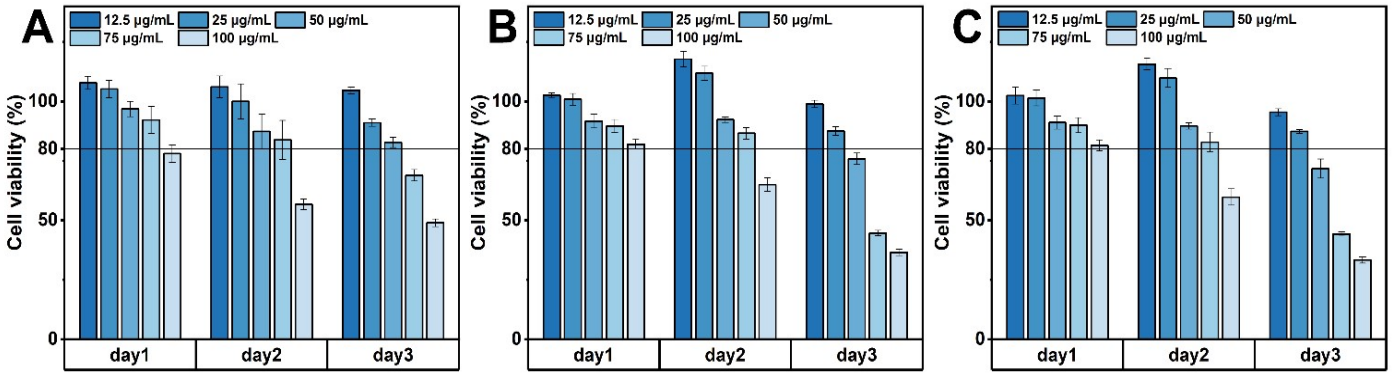

Figure S13. Cytotoxicity results of HUVEC cells by CCK-8 assay: (A) AuM, (B) T-AuM and (C) CT-AuM

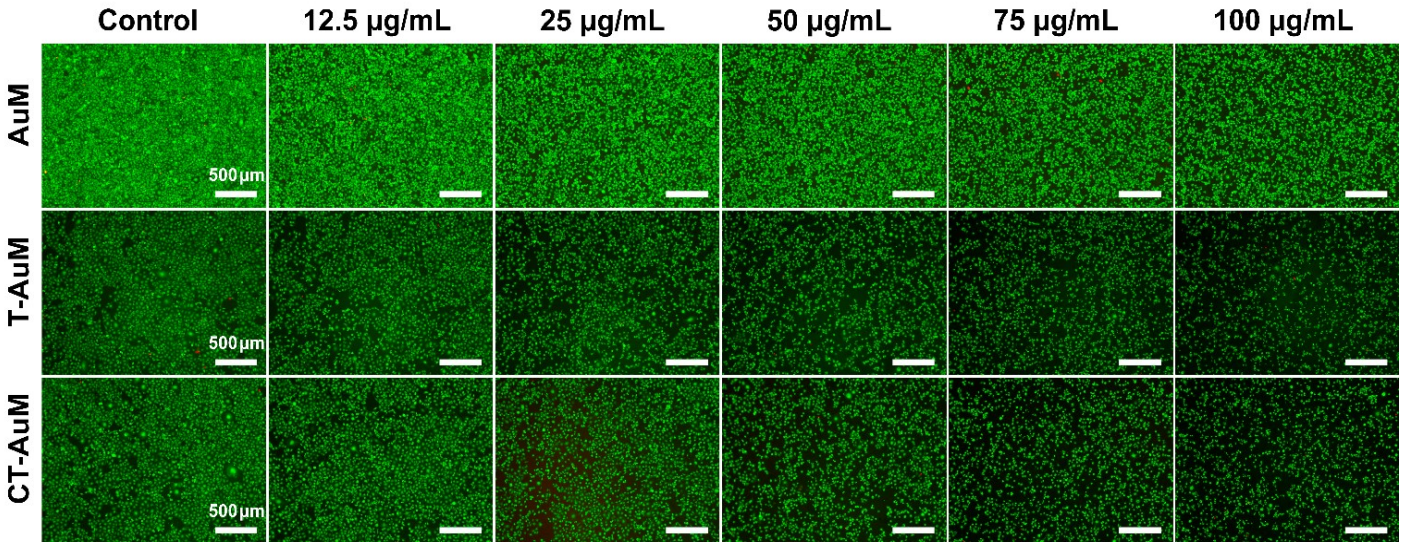

Figure S14. Live/dead staining (Calcein-AM/PI) images of HUVEC cells at day 1

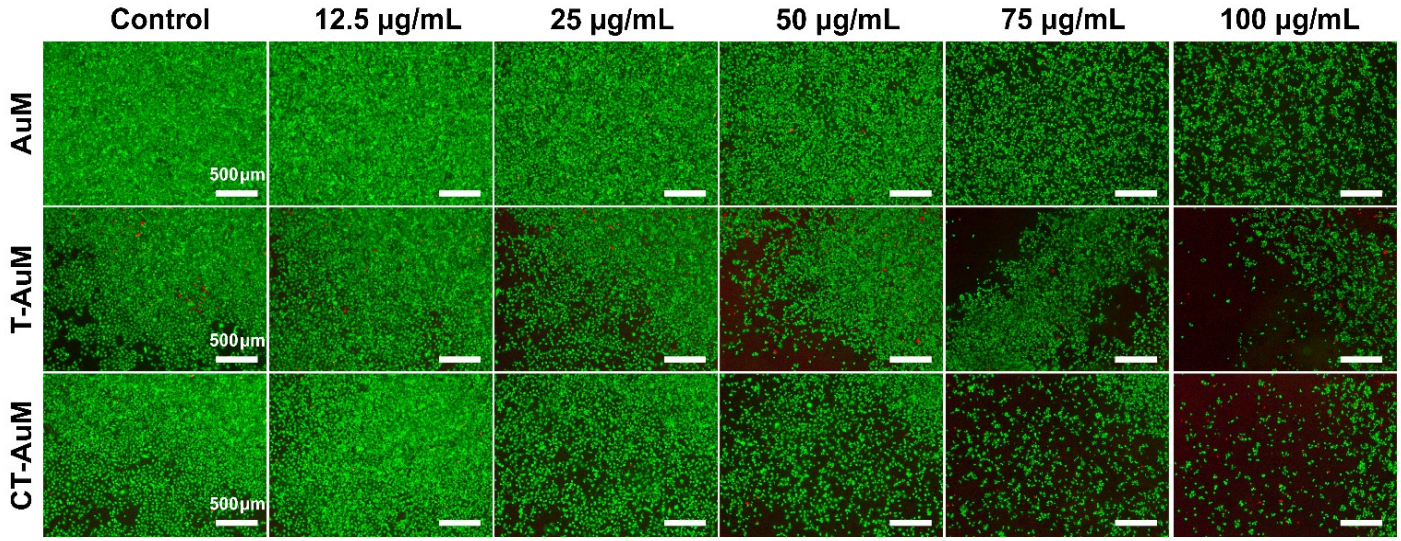

Figure S15. Live/dead staining (Calcein-AM/PI) images of HUVEC cells at day 2

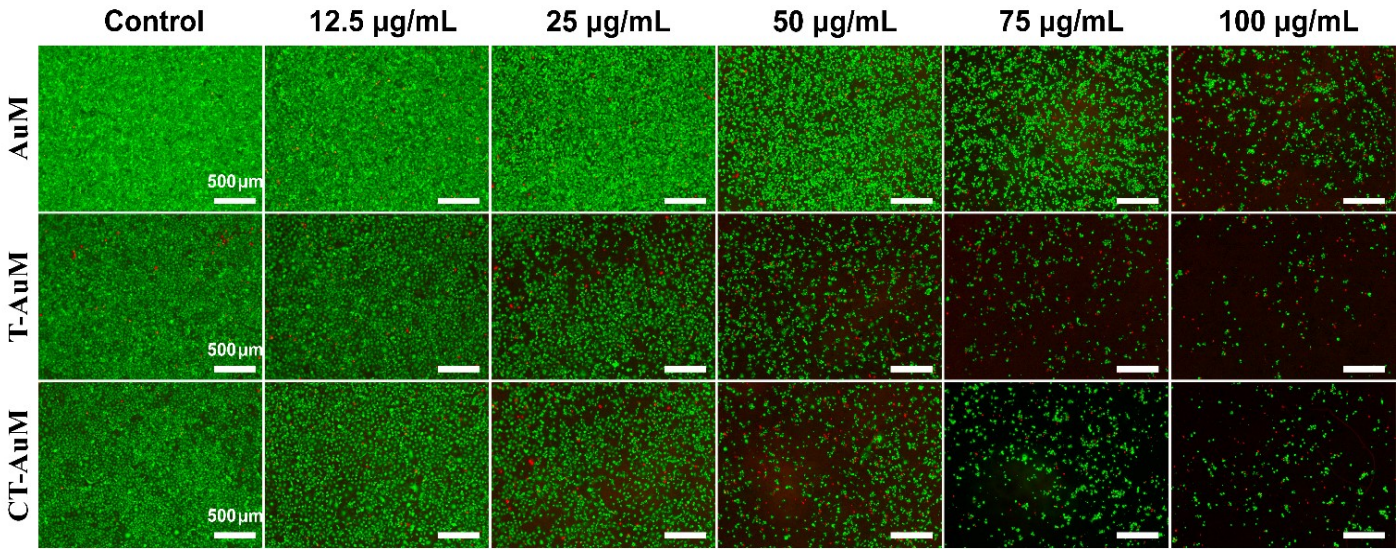

Figure S16. Live/dead staining (Calcein-AM/PI) images of HUVEC cells at day 3

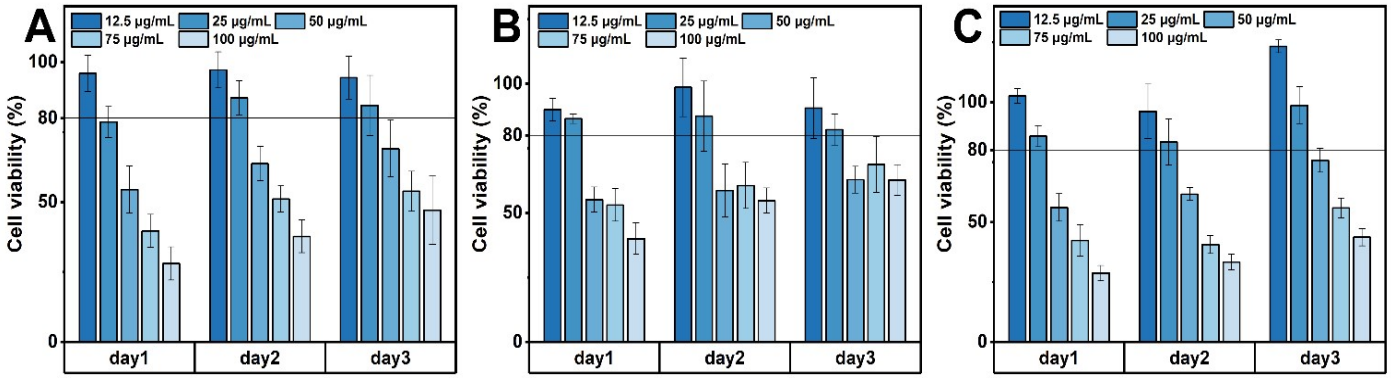

Figure S17. Cytotoxicity results of RAW264.7 cells by CCK-8 assay: (A) AuM, (B) T-AuM and (C) CT-AuM

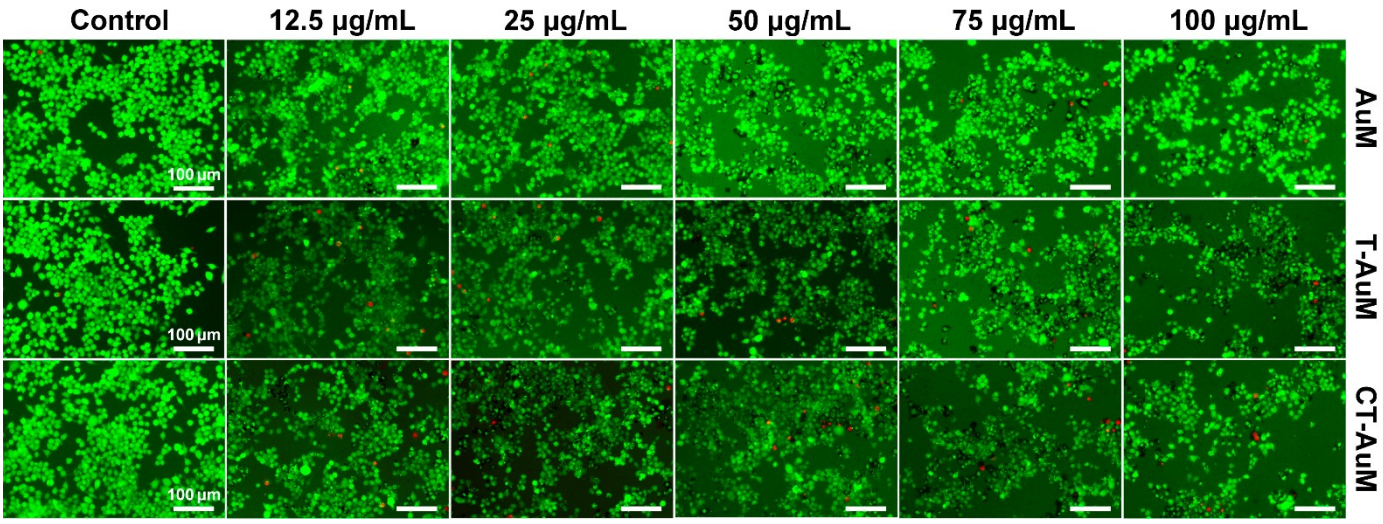

Figure S18. Images of RAW264.7 cells with live/dead staining (Calcein-AM/PI) at day 1

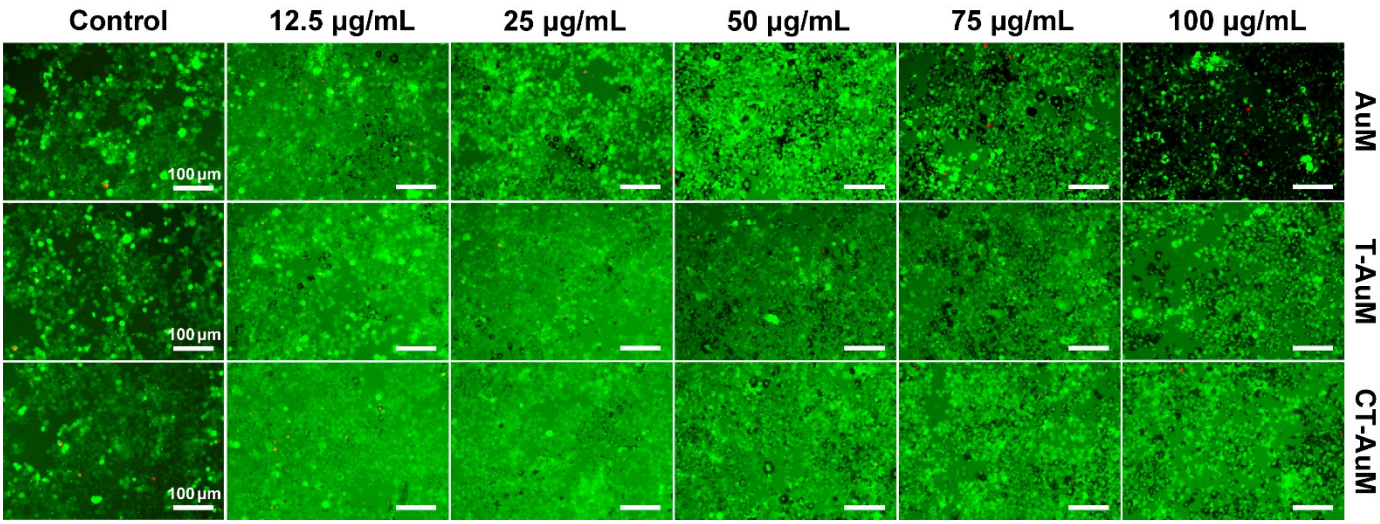

Figure S19. Images of RAW264.7 cells with live/dead staining (Calcein-AM/PI) at day 2

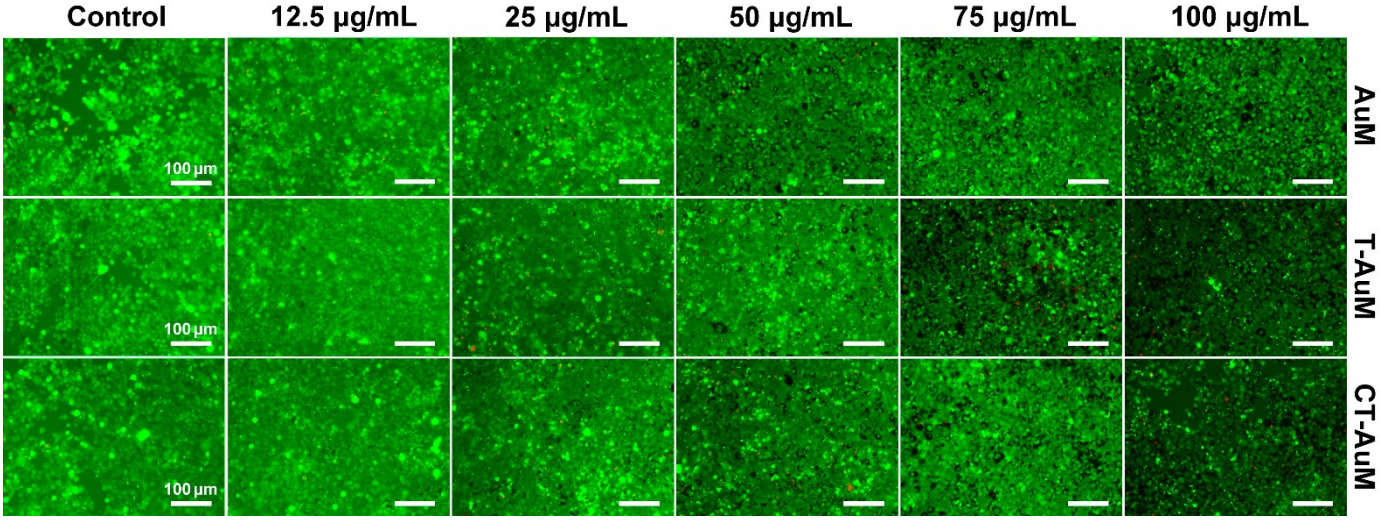

Figure S20. Images of RAW264.7 cells with live/dead staining (Calcein-AM/PI) at day 3

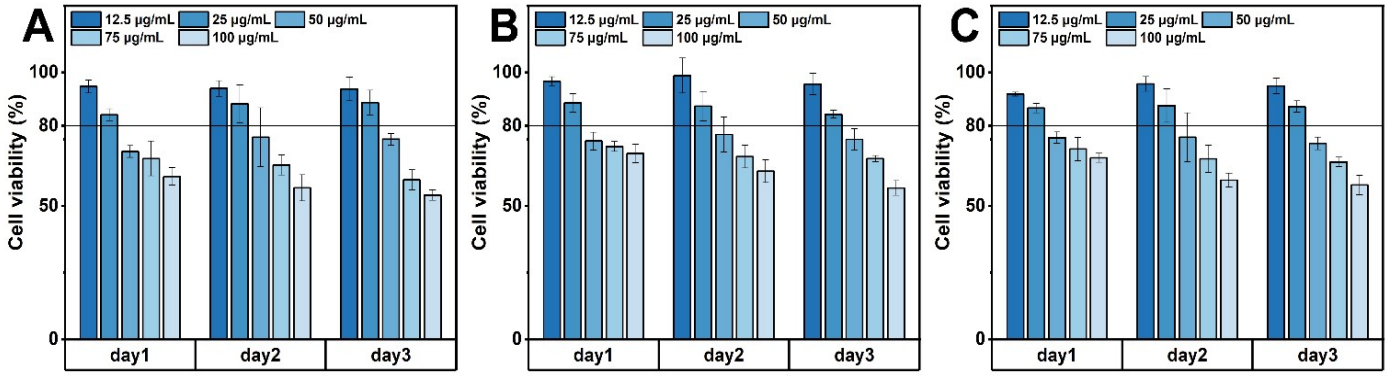

Figure S21. Cytotoxicity results of VSMC cells by CCK-8 assay: (A) AuM, (B) T-AuM and (C) CT-AuM

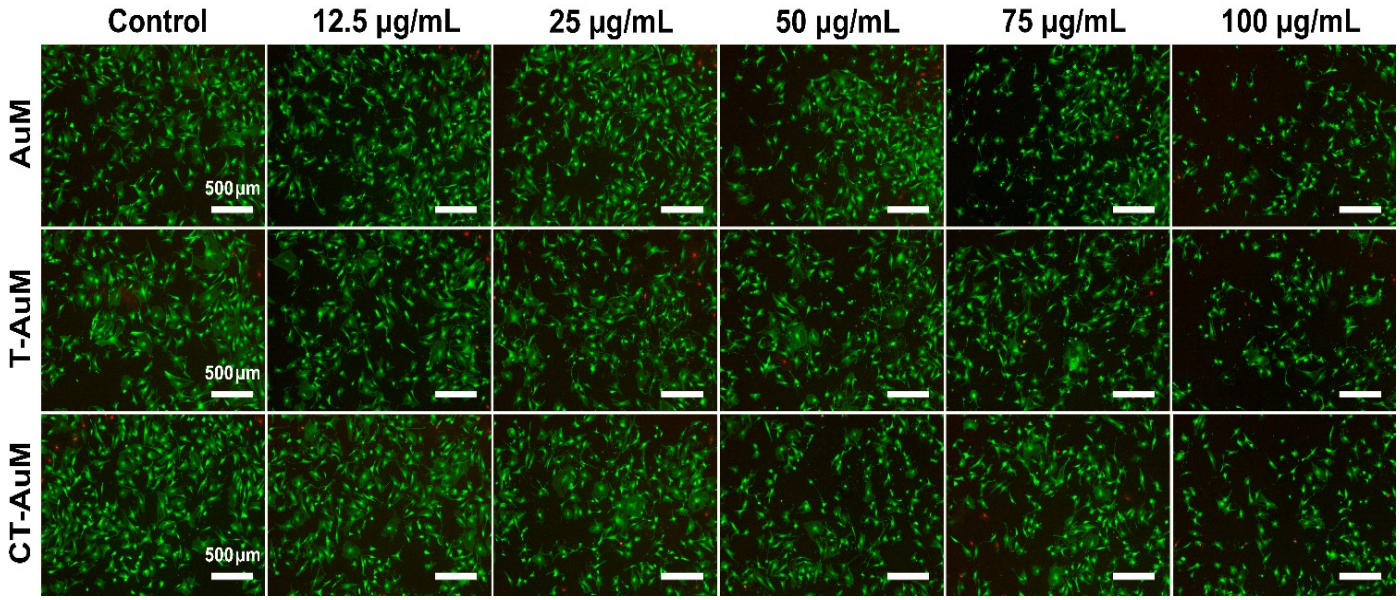

Figure S22. Images of VSMC cells of live/dead staining (Calcein-AM/PI) at day 1

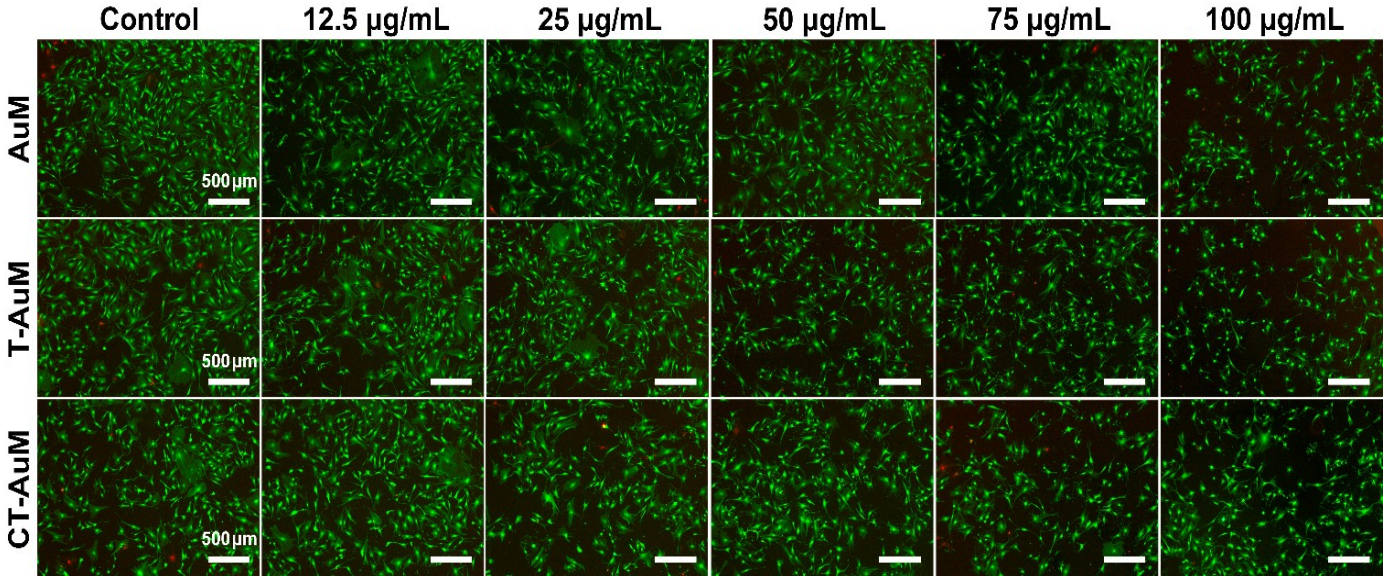

Figure S23. Images of VSMC cells of live/dead staining (Calcein-AM/PI) at day 2

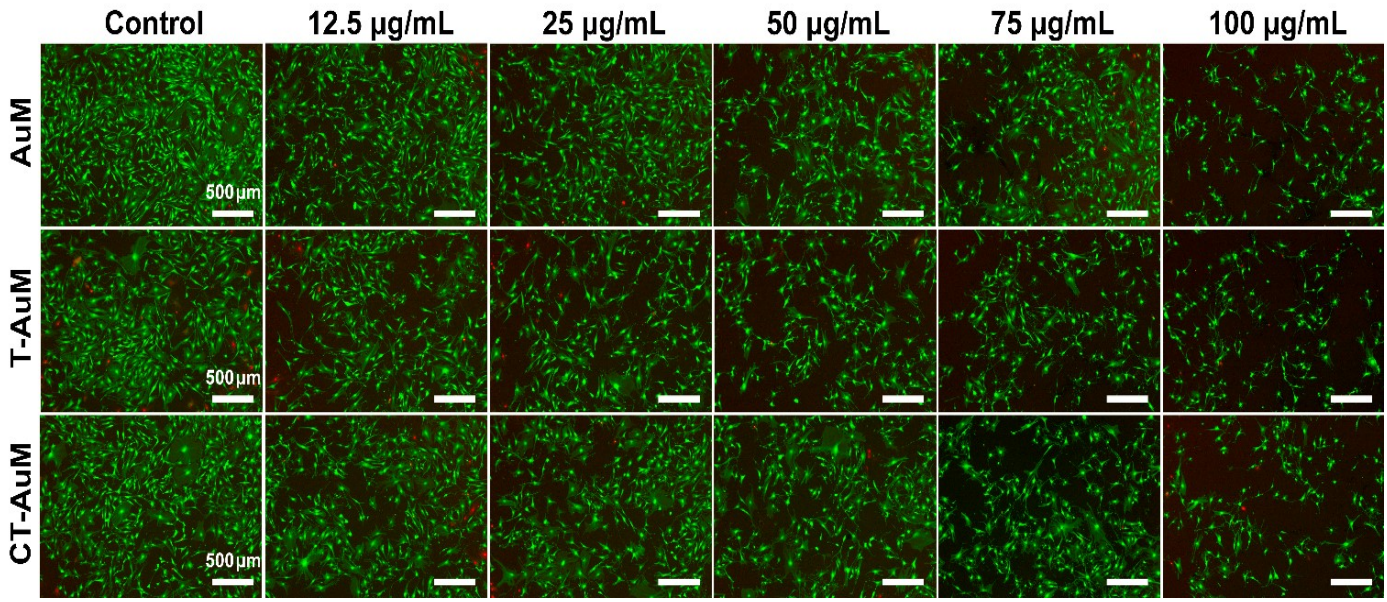

Figure S24. Images of VSMC cells of live/dead staining (Calcein-AM/PI) at day 3

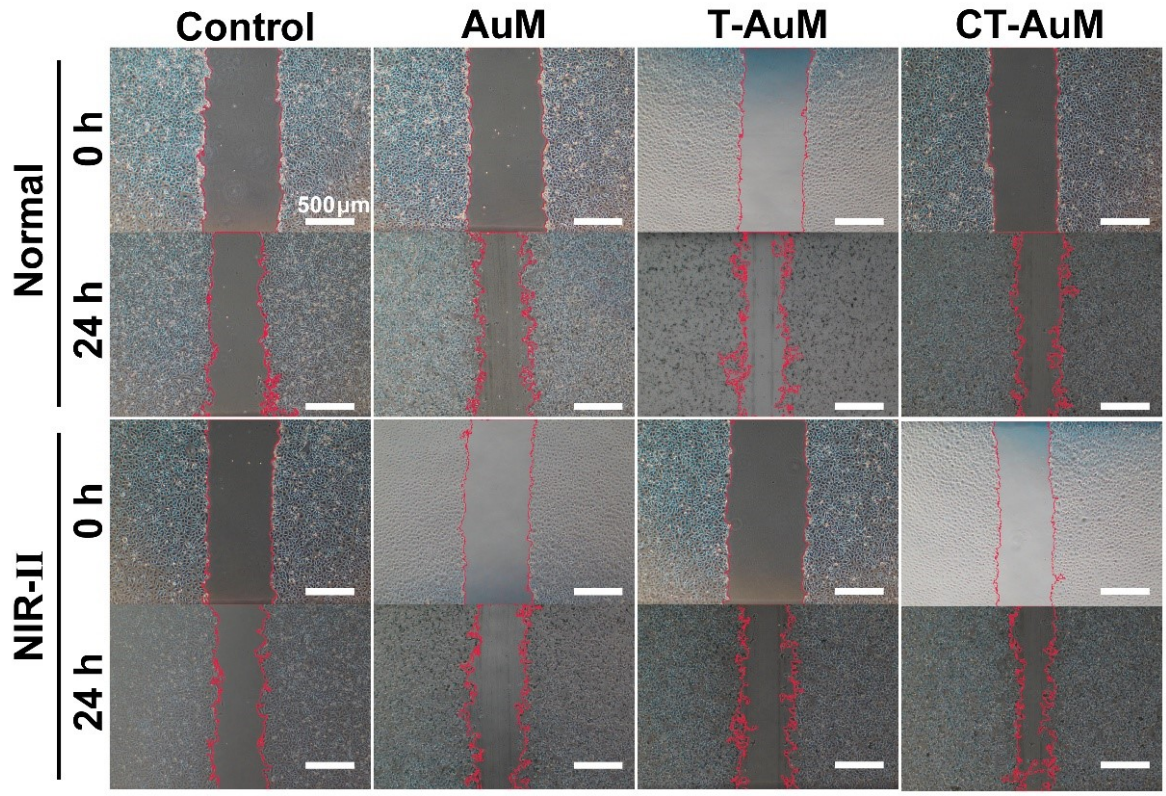

Figure S25. Cell images of the wound healing (scratch) assay for HUVECs

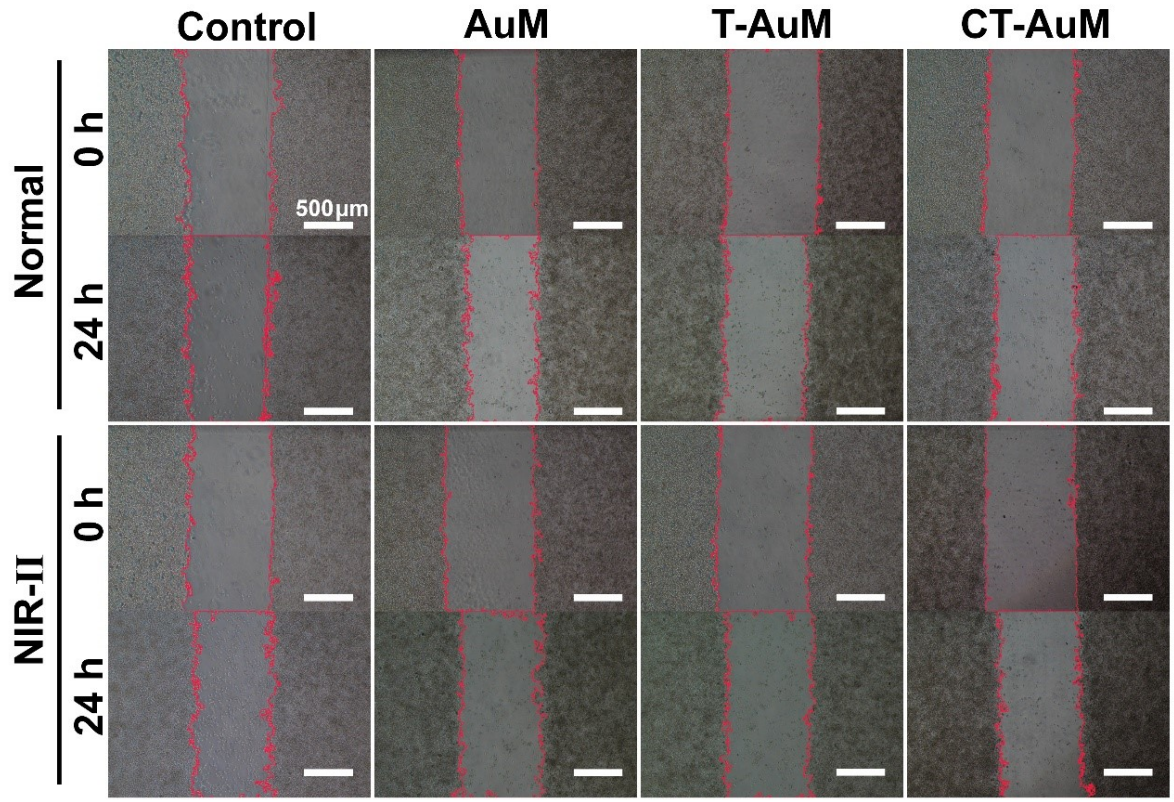

Figure S26. Cell images of the wound healing (scratch) assay for RAW264.7

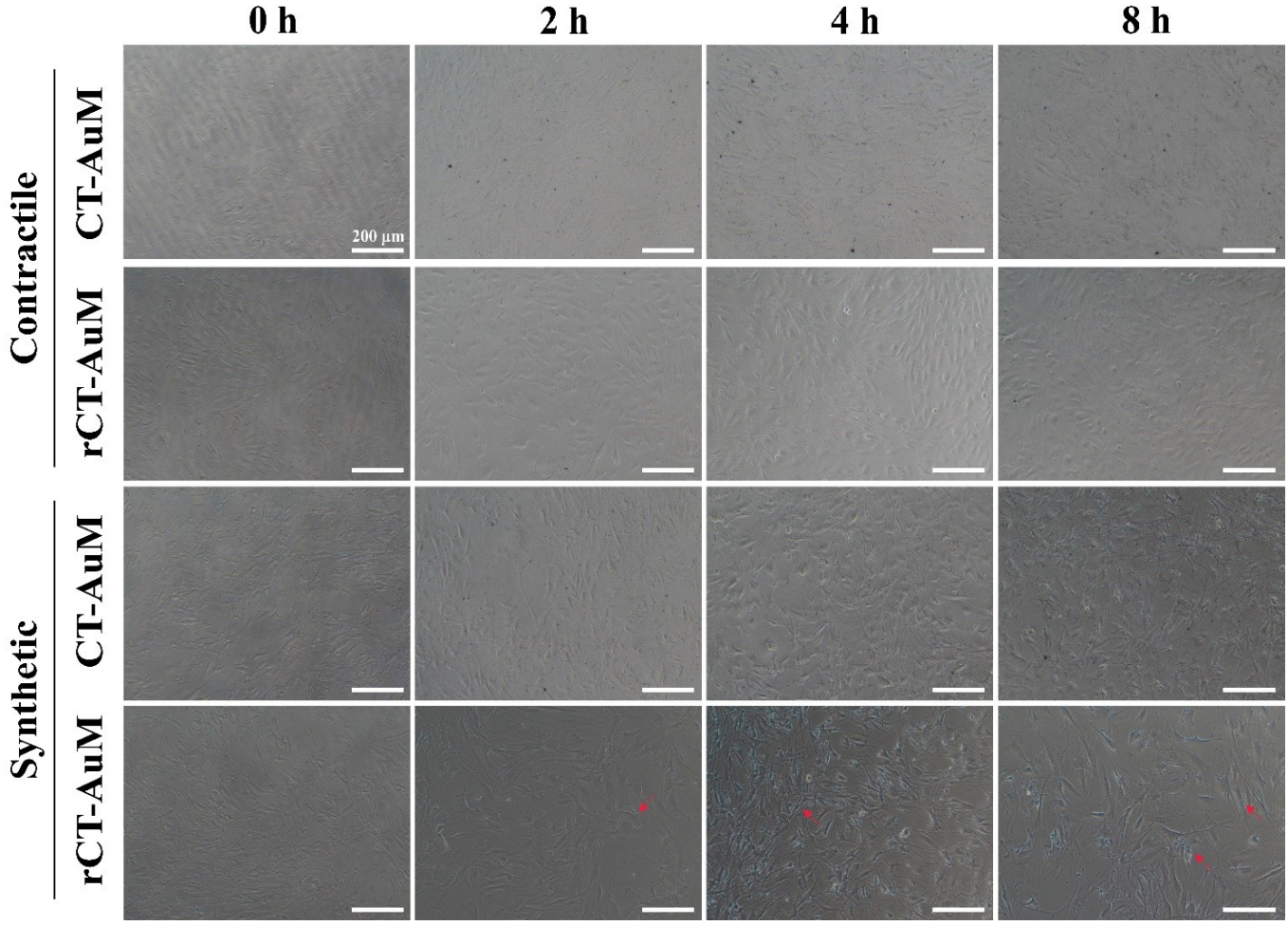

Figure S27. Images of contractile and synthetic VSMCs uptake of CT-AuM and rCT-AuM

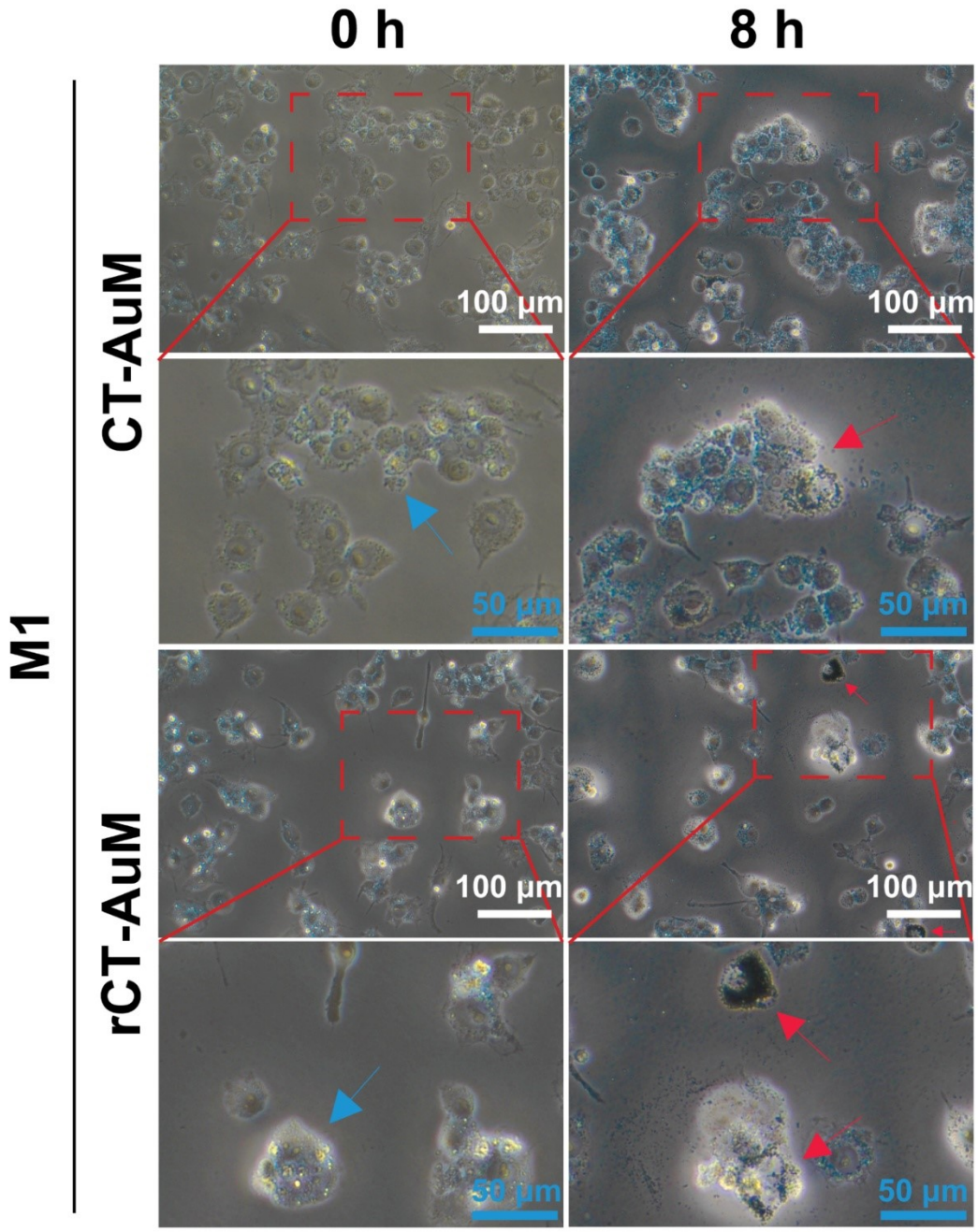

Figure S28. Comparative magnified views of material uptake efficiency by RAW264.7 at 0 and 8 h (Blue arrows indicate that at 0 h, the cells had taken up negligible amounts of material; red arrows indicate regions of material accumulation)

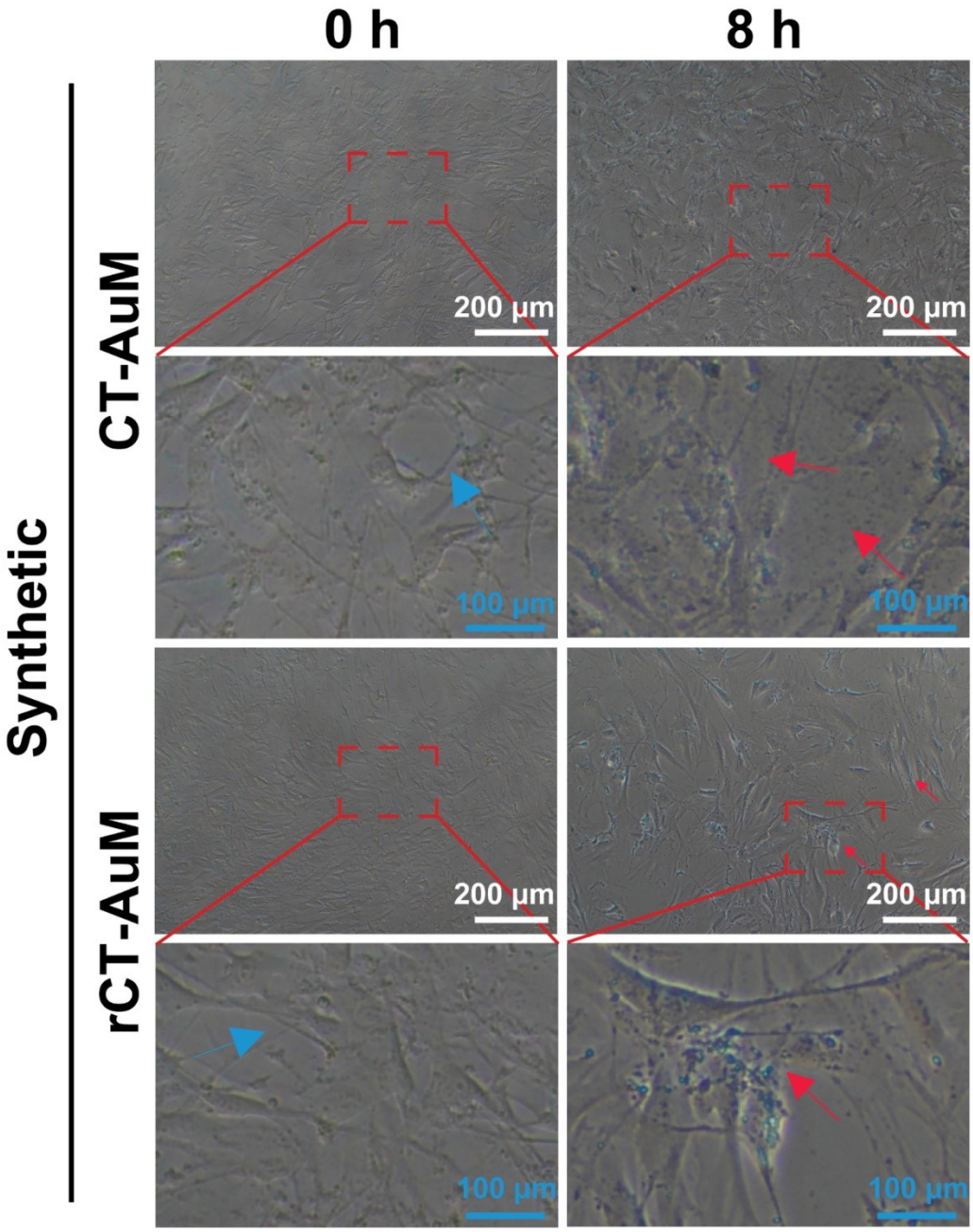

Figure S29. Comparative magnified views of material uptake efficiency by VSMCs at 0 and 8 h (Blue arrows indicate that at 0 h, the cells had taken up negligible amounts of material; red arrows indicate regions of material accumulation)

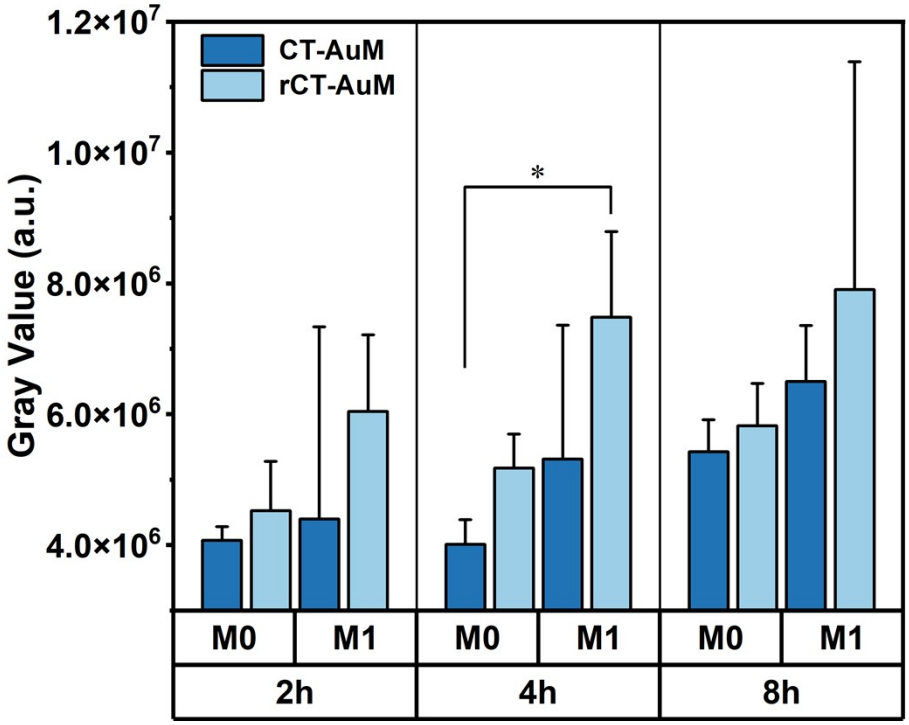

Figure S30. Semi-quantitative analysis of the uptake of CT-AuM and rCT-AuM by M0/M1 RAW264.7

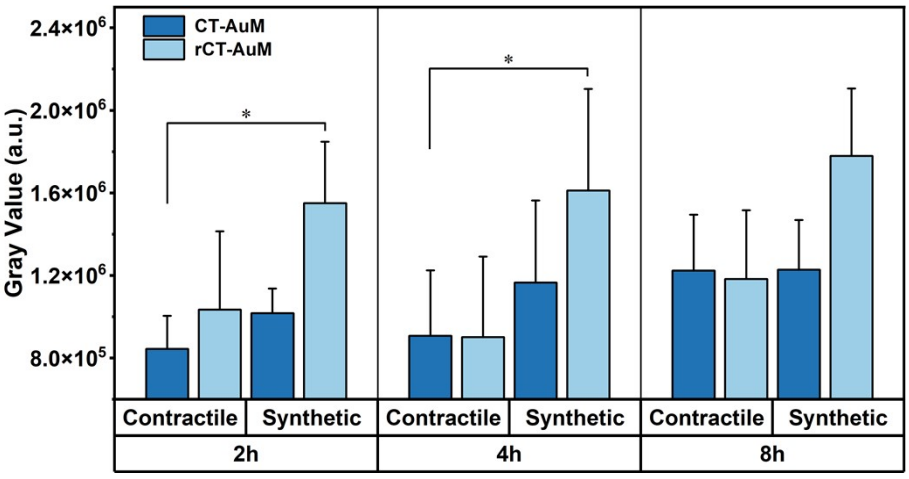

Figure S31. Semi-quantitative analysis of the uptake of CT-AuM and rCT-AuM by contractile/synthetic VSMCs

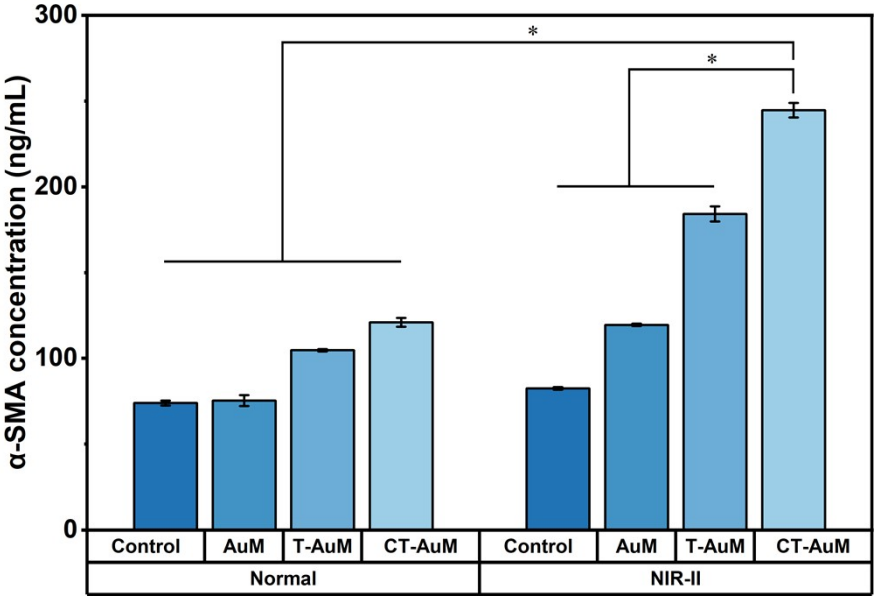

Figure S32. Expression level of α-SMA in VSMCs lysates of different materials

Due to certain fluctuations among parallel samples of in vivo animal data that did not meet the assumption of homogeneity of variance, the ultrasound-related data are presented as the median of six parallel samples per group. Figures S32, S34, and S35 show representative images from a single sample.

Table S3. Ultrasonographic data of AAA mice before treatment

group	maximum average aortic diameter (mm)	circumferential cyclic strain (%)	blood flow velocity (mm/s)
Normal 1	0.638	21.19	123.1
Normal 2	0.593	20.22	131.5
Normal 3	0.644	23.06	215.9
Normal 4	0.665	17.78	207.7
Normal 5	0.662	19.87	216.7
Normal 6	0.589	16.91	128.2
AAA 1	0.893	1.764	40.778
AAA 2	0.880	2.882	42.022
AAA 3	0.776	4.981	37.377
AAA 4	0.773	3.269	30.104
AAA 5	0.717	1.277	35.114
AAA 6	0.685	0.426	34.302

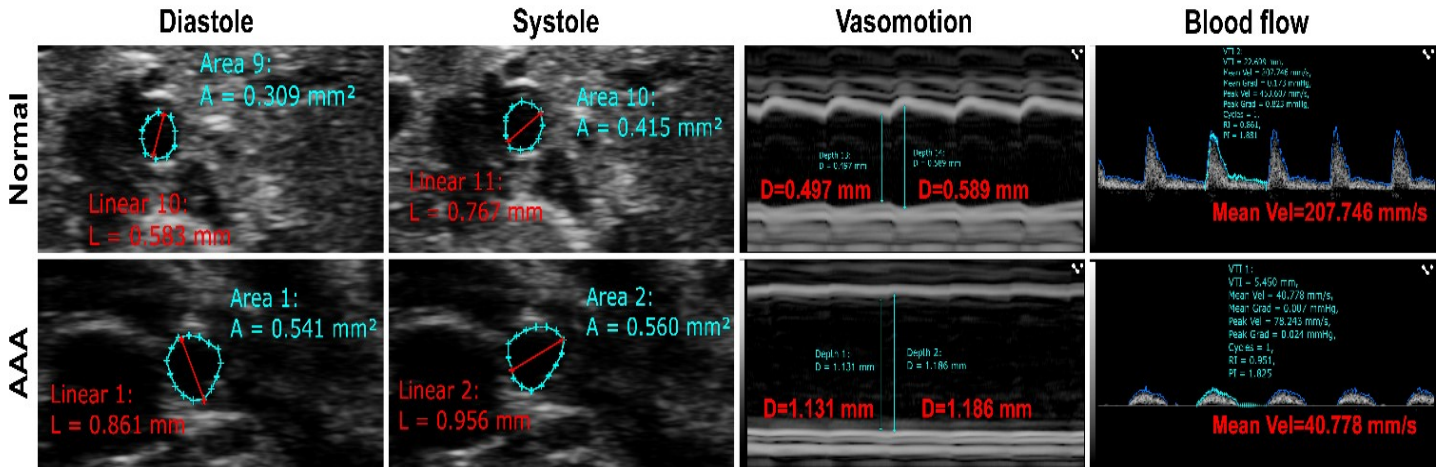

Figure S33. Pre-treatment ultrasound imaging evaluation in AAA mice (Representative images)

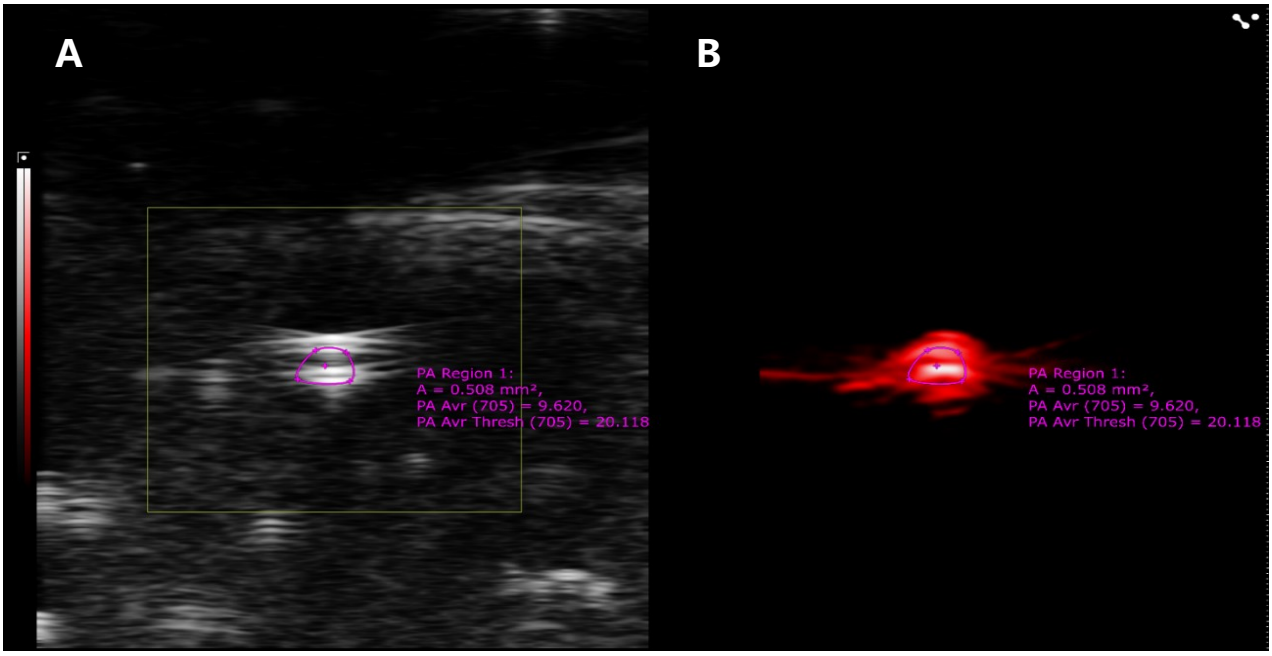

Figure S34. Ultrasound and photoacoustic imaging of rCT-AuM: (A) Ultrasound (US) image; (B) Photoacoustic (PA) image

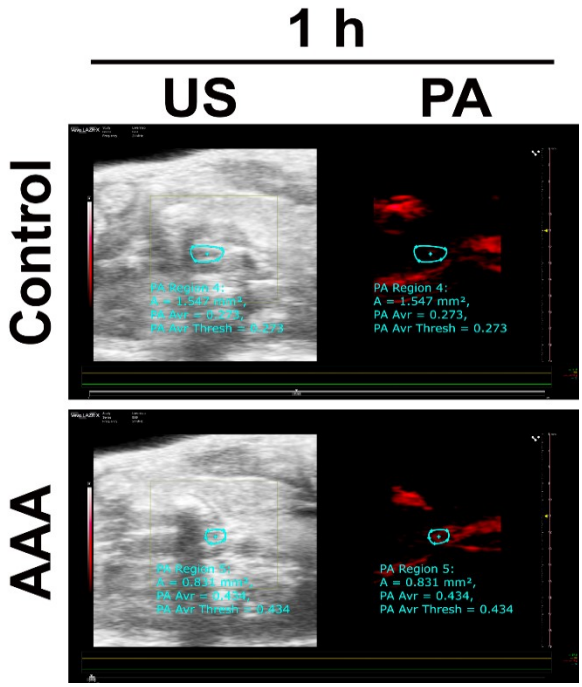

Figure S35. In vivo ultrasound-photoacoustic imaging of mice at 1 h post-injection of rCT-AuM (Representative images)

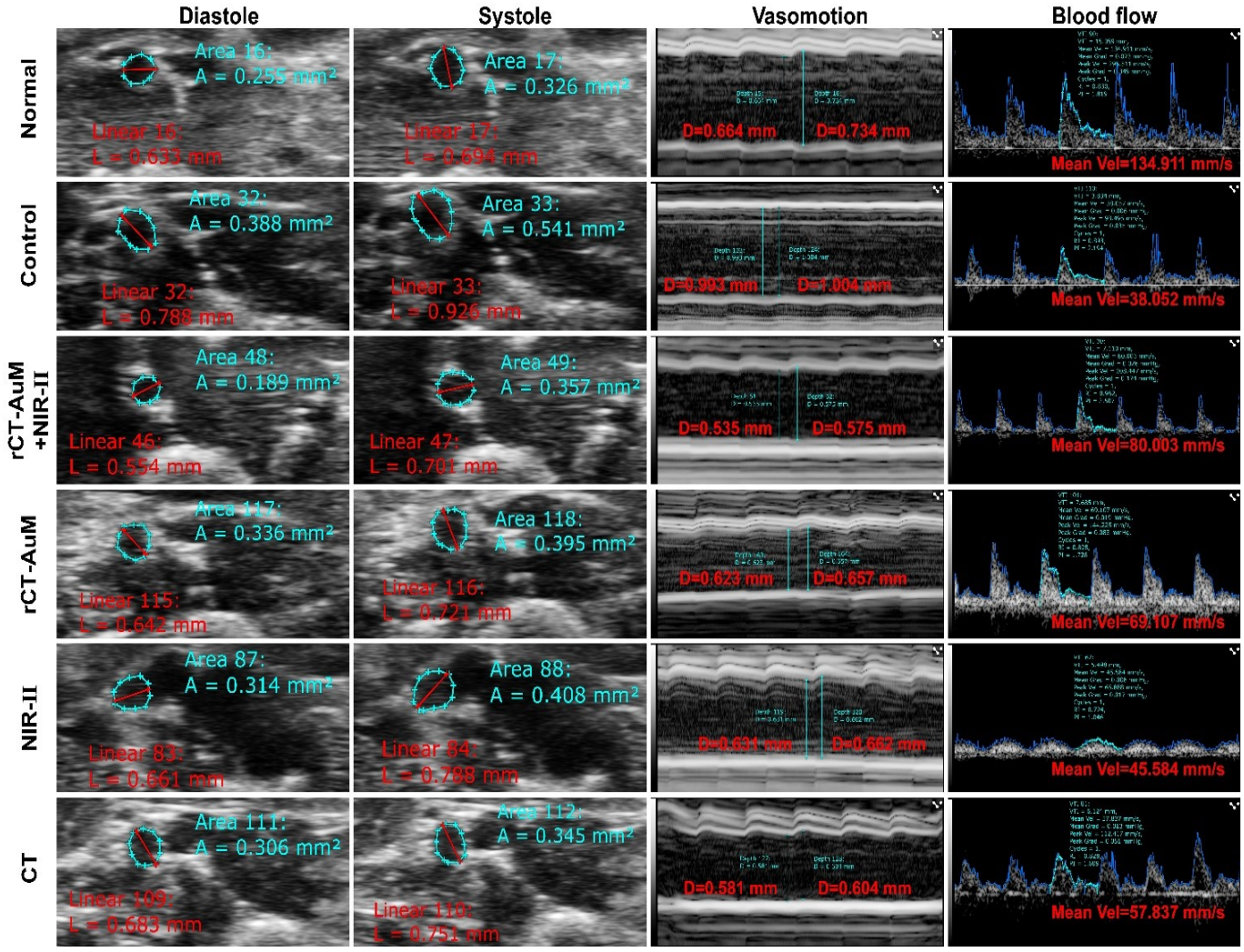

Figure S36. Post-2-week treatment ultrasound imaging evaluation in AAA mice (Representative images)

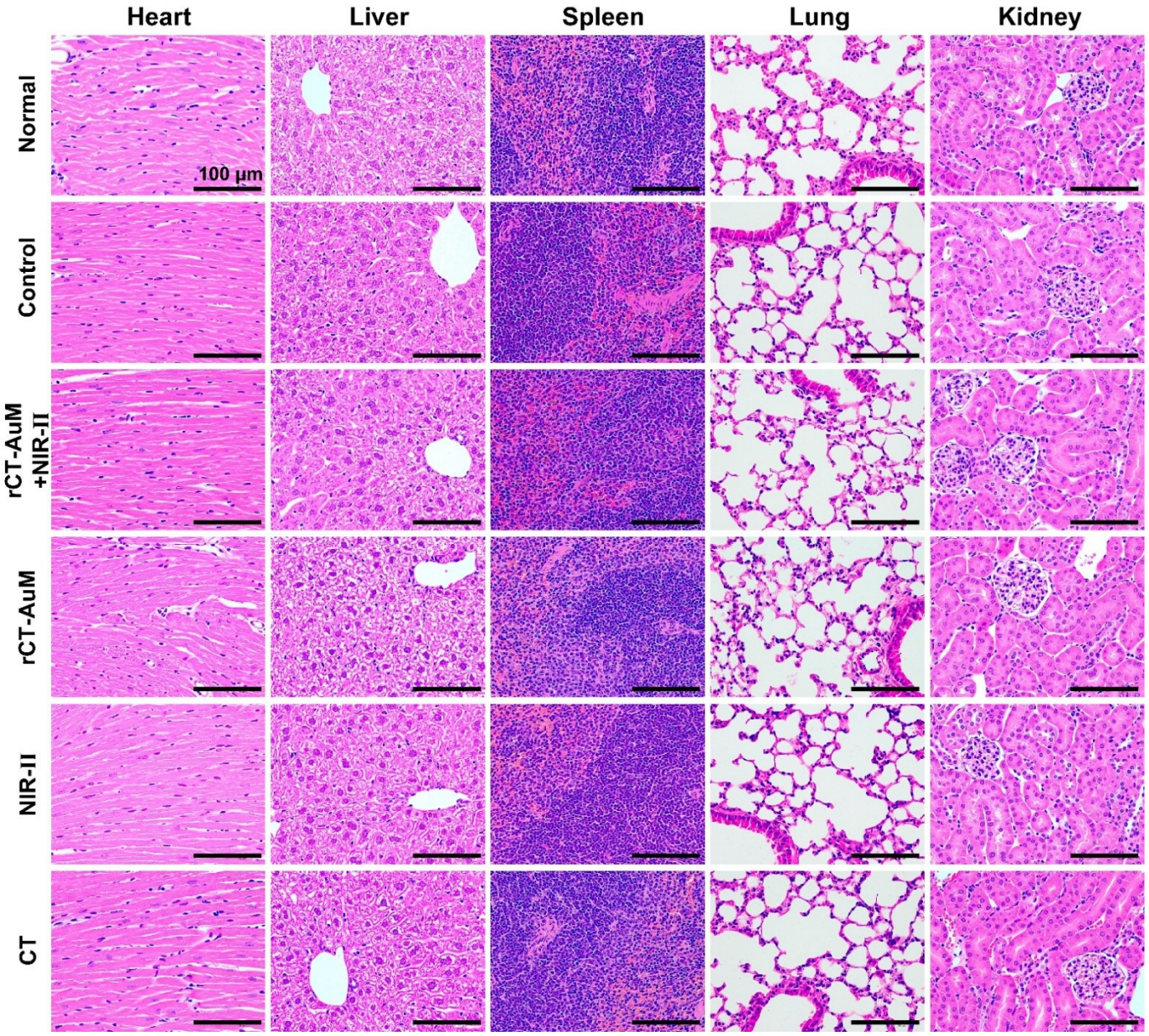

Figure S37. H&E-stained tissue section images of various organs from each group of animals

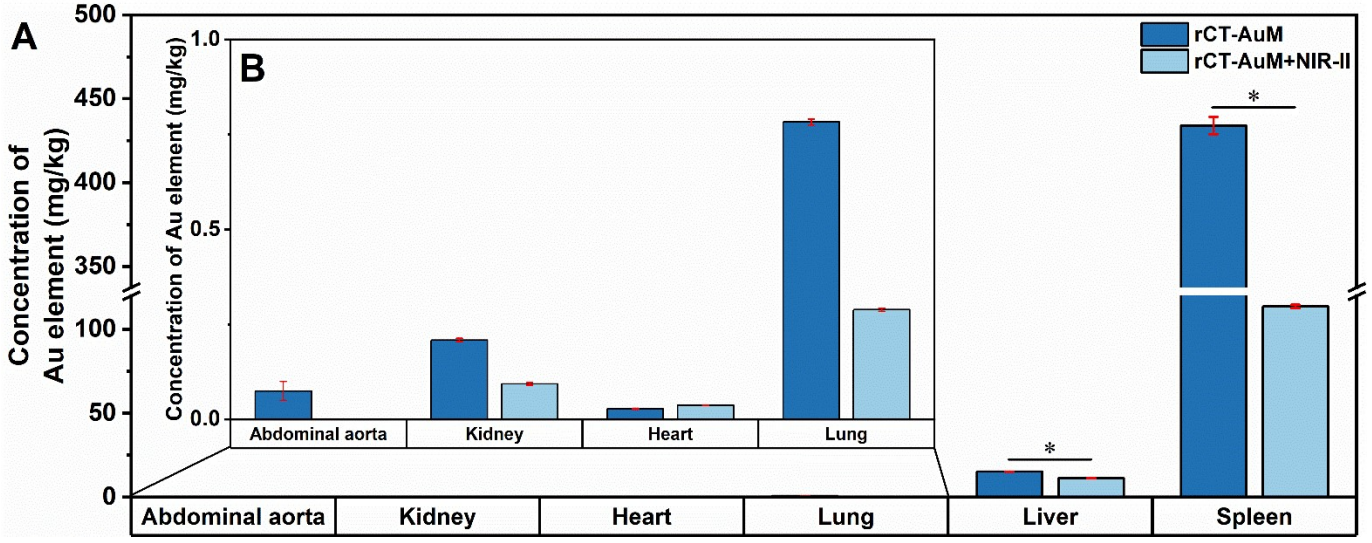

Figure S38. (A) Gold content in different organs of mice after treatment: abdominal aorta, kidney, heart, lung spleen and liver; (B) Enlarged view of abdominal aorta, kidney data, heart and lung

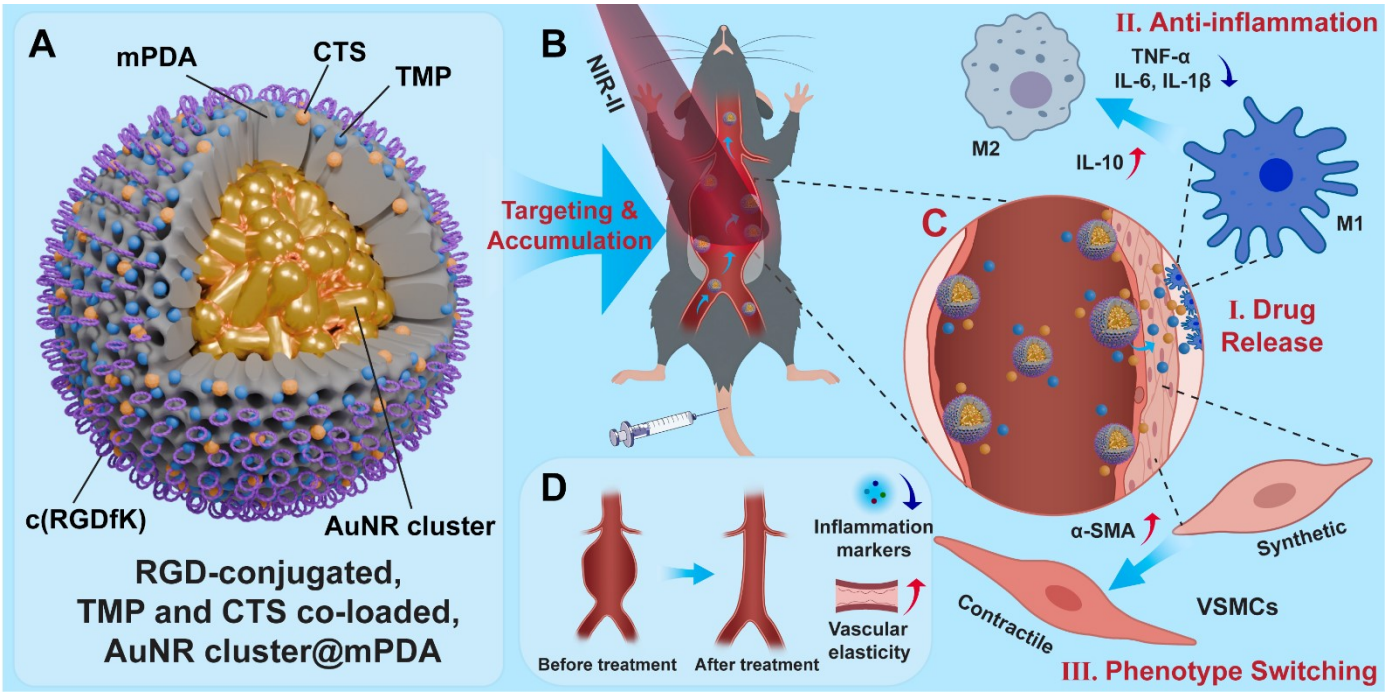

Figure S39. Schematic on the construction, targeted delivery and synergistic therapeutic mechanism of rCT-AuM nanosystem for AAA treatment: (A) Structure of rCT-AuM; (B) Targeted accumulation of rCT-AuM in AAA lesion region; (C) NIR II irradiation triggered synergistic therapy: (I) photothermal conversion and controlling drug release; (II) released drugs inhibit M1 macrophage polarization and modulate inflammatory cytokines; (III) drug induced reversion of vascular smooth muscle cells to a contractile phenotype with up regulated a-SMA expression. (D) Combined rCT-AuM + NIR-II therapy synergistically inhibits aortic dilation and improves vascular wall structure and function through above multi mechanistic actions

References

1 Q. Tian, F. Jiang, R. Zou, Q. Liu, Z. Chen, M. Zhu, S. Yang, J. Wang, J. Wang and J. Hu, *ACS Nano*, 2011, **5**, 9761-9771.

2 M. Gao, H. Zhao, Z. Wang, Y. Zhao, X. Zou and L. Sun, *Adv. Powder Technol.*, 2021, **32**, 1972-1982.

3 E. H. Phillips, A. A. Yrineo, H. D. Schroeder, K. E. Wilson, J. Cheng and C. J. Goergen, *Biomed Res. Int.*, 2015, **2015**, 1-12.